LED illumination for planar PIV in large-scale hydraulic laboratories

Bakker, Wout; de Fockert, Anton; Nogueira, Helena I.S.; Oldenziel, Gosse

DOI
10.1016/j.flowmeasinst.2025.103093

Publication date
2026

Document Version
Final published version

Published in
Flow Measurement and Instrumentation

Flow Measurement and Instrumentation 107 (2026) 103093

Contents lists available at ScienceDirect

Flow Measurement and Instrumentation

journal homepage: www.elsevier.com/locate/flowmeasinst

LED illumination for planar PIV in large-scale hydraulic laboratories

Wout Bakker [a,b,1,*], Anton de Fockert [a], Helena I.S. Nogueira [a], Gosse Oldenziel [a,c]

[a] Deltares, PO Box 177, 2600MH, Delft, the Netherlands
[b] Hydraulic Engineering Laboratory, CiTG faculty, Delft University of Technology, Delft, the Netherlands
[c] Laboratory for Aero- and Hydrodynamics, 3mE faculty, Delft University of Technology, Delft, the Netherlands

ARTICLE INFO

Keywords:
Light emitting diodes
Particle image velocimetry
Large-scale hydraulic laboratories
LED-Based PIV
Motion blur

ABSTRACT

This paper presents the application, and implications of line arrays of light emitting diodes (LEDs) as an illumination source for planar particle image velocimetry (PIV) measurements in large-scale hydraulic laboratories. The use of class 4 lasers, commonly applied as illumination source in these PIV measurements, requires strict safety precautions (i.e. to prevent safety hazards for people working in their vicinity), specifically when applied at hydraulic experimental setups that are not located in a laser lab. To examine the applicability of an alternative light source, differences between LED- and laser-based illumination for PIV are analyzed. A theoretical analysis, in which a so-called motion blur parameter (β_{mb}) is introduced, shows that for moderate flow velocities in large-scale setups, image blur can be avoided, even for relatively long (millisecond) pulse widths. The light sheet thickness, width and intensity of a pulsed laser and a line array of both continuous and pulsed LEDs are measured and compared. Based on these properties a safety assessment is made, from which it is concluded that the application of arrays of LEDs for PIV measurements applied in liquid flows requires significantly less safety precautions than in case a class 4 PIV laser is used. Planar (2D) PIV measurements have been performed with both a pulsed and a continuous LED as light source for two testcases in large hydraulic scale-models. Time-averaged velocity field results from the LED-based PIV measurements show good resemblance to both PIV measurements obtained with a class 4 laser as well as to pitot tube measurements. It is shown that the time-averaged PIV vector fields are influenced by motion blur, resulting in a distinct bias towards smaller velocities when increasing motion blur. The two testcases show that linear LED arrays can serve as a suitable alternative illumination source for planar PIV measurements in large-scale hydraulic laboratories in case motion blur remains limited. Specifically, LED line arrays are considered useful for the time-average quantification of predominantly 2D, low to moderate flows in a relatively large domain.

List of symbols

A_0	light emitting area at light source	[m^2]
A_p	area of emitted light sheet bundle	[m^2]
A_{ref}	area of diffusive reflected area	[m^2]
B	blue-light hazard weighting function	[−]
β_{mb}	motion blur parameter	[−]
D_i	internal pipe diameter	[m]
D_I	interrogation window size	[pix]
d_τ	particle image diameter	[m]
d_r	pixel size	[m]
Δt	interframe time of PIV measurement	[s]
ΔX_p	interframe particle displacement in interrogation window	[%]
f_p	repetition rate of pulsed light source	[Hz]
$f^\#$	f-number of camera lens	[−]
H_e	radiant exposure of light at receiver	[J/m^2]
H_p	radiant exposure of particle	[J/m^2]
H_{ref}	reflected radiant exposure of laser	[J/m^2]
I_p	imaged intensity on target	[arb.]
k	multiplication factor for unknown laser mode structure	[−]
l_l	additional illuminated particle image length	[m]
L_e	radiance of emitted light at specific point	[W/m^{2}sr]
L_B	effective blue-light radiance of LED	[W/m^{2}sr]
L_B^{EL}	exposure limit of blue-light radiance of LED	[W/m^{2}sr]
L_R	effective retinal thermal radiance of LED	[W/m^{2}sr]
L_R^{EL}	exposure limit of thermal radiance of LED	[W/m^{2}sr]
L_{skin}	skin thermal radiance of LED	[W/m^{2}sr]

(continued on next column)

(continued)

(continued on next page)

* Corresponding author. Deltares, PO Box 177, 2600MH, Delft, the Netherlands.
E-mail address: info@ecoflowsadvies.nl (W. Bakker).
[1] currently: EcoFlows, Amsterdam, the Netherlands.

https://doi.org/10.1016/j.flowmeasinst.2025.103093
Received 30 May 2025; Received in revised form 2 October 2025; Accepted 20 October 2025
Available online 31 October 2025

(*continued*)

λ	wavelength of emitted light	[nm]
M_0	lateral magnification of optical system	[−]
Ω_s	solid angle of emitted light bundle	[sr]
Φ_e	radiant flux emitted by light source	[W]
$\Phi_{e,\lambda}$	spectral radiance of emitted light	[W/m^2 · sr· nm]
Φ_v	luminous flux emitted by light source	[lm]
ρ_s	mass density of tracer particle	[kg/m^3]
Q	flow discharge	[l/s]
Q_e	radiant energy emitted by light source	[J]
Q_s	radiant energy reflected by extended source	[J]
R	retinal thermal hazard weighting function	[−]
R_i	reflectance of material I	[−]
R^2	coefficient of determination	[−]
r	radius of curvature of LED lens	[m]
τ_p	pulse width of light source	[s]
u	streamwise velocity component	[m/s]
u_p	tracer particle velocity	[m/s]
u'_{RMS}	root-mean-square of velocity fluctuations from PIV time series	[m/s]
$\overline{u}$	time-averaged velocity from PIV time series	[m/s]
w	vertical velocity component	[m/s]
w_{pipe}	pipe bulk velocity	[m/s]
w_{avg}	spatially and time-averaged vertical velocity in suction pipe	[m/s]
x	streamwise location in test setups	[m]
x_{ref}	distance between reflecting light source and target	[m]
x_s	distance between light source and target	[m]
y	vertical location in test setup	[m]
y_0	width of light source	[m]
y_p	width of emitted light sheet bundle	[m]
z_0	thickness/height of light source	[m]
z_p	mean thickness of emitted light sheet bundle	[m]
$z_{p,s}$	thickness of emitted light sheet bundle at specific y-location	[m]
θ	divergence angle of emitted light sheet thickness	[rad]
φ	divergence angle of emitted light sheet width	[deg]
φ_{ref}	divergence angle of reflected light	[deg]

1. Introduction

To assess the hydrodynamic performance of hydraulic structure designs (e.g. for pump stations, navigational locks, break waters, weirs) flow characteristics should be investigated. This can be based on theoretical analysis, expert judgement, numerical modeling, flow quantification in physical scale-models or field work campaigns. Developments in computational possibilities in the last decades resulted in an increased use of numerical modelling techniques -such as computational fluid dynamics (CFD) simulations-as a design tool for hydraulic structures. However, generally CFD-simulations of (turbulent) flows are based on approximations of flow phenomena at small scales to reduce computational costs [1]. Under certain conditions, these approximations can introduce uncertainties and/or inaccuracies in the CFD results such that physical model tests are needed for verification [2]. In large physical scale-models (i.e. experimental setups with dimensions in the order of meters) flow quantification is conventionally performed using (intrusive) point measurement methods, such as pressure sensors, pitot tubes, electromagnetic flow sensors (EMS), laser Doppler velocimetry (LDA/LDV) and acoustic Doppler velocimetry (ADV) [2,3]. In recent years the application of 2D and 3D optical measurement techniques, such as particle image velocimetry (PIV) for these validation purposes strongly increased [4]. In contrast to the experimental measurement techniques mentioned above, PIV has the advantage being non-intrusive and providing high-resolution instantaneous quantification of 2D or 3D flow fields, which generally provides more information and understanding of the investigated flows than measurements obtained with point probes.

PIV is an optical measurement technique that is widely applied in academic research [5]. This work focusses on *planar* PIV measurements, with which two components of the velocity in a two-dimensional surface (plane) of a flow can be obtained (also known as *2D2C* PIV). Conducting a two-component planar PIV measurement requires an illumination source, a (double frame) camera, tracer particles and optical access to the flow. Due to their high radiance and ability to generate collimated and coherent light, pulsed lasers are the standard as illumination source in a PIV system [4]. For a planar PIV measurement, the laser beam is expanded by a (set of) lens(es) to form a thin light sheet. Suspended tracer particles (which are assumed to follow the flow) that are located in the light sheet, reflect the laser light, which is imaged by the camera's sensor. This procedure is performed two consecutive times with an interframe-time Δt, resulting in two frames or a *frame pair* both representing an image field consisting of a large number of particle reflections. Each image is subdivided in regions (interrogation windows) in which the mean displacement of all the particles in that particular region is derived applying spatial cross correlation of the two image fields of each frame pair. This results in a field of two components of the instantaneous flow velocity throughout the imaged region.

Laser-based PIV is applied for a wide variety of research purposes, from micro-PIV (with measurement regions in the order of mm^2) up to large-scale PIV (measurement regions in the order of 1 × 1 m^2) [4], where larger measurement domains generally demand more laser power. The application of high-power lasers brings along the risk of eye- or skin damage from high intensity light exposure [6]. Therefore, experiments with class 4 lasers are commonly conducted in facilities which are designed specifically for this task (such as an optical laboratory), which are only accessible by certified personnel (laser safety officers). However, for experiments in setups of large physical scale-models this is impractical as strict laser safety precautions have to be met [6], such as laser-safe shielding of experimental setups, or closing of the surrounding region, which are time consuming, impractical and costly interventions (see Fig. 1). Moreover, high-power (pulsed) lasers are expensive, complex and delicate instruments vulnerable for contamination, which make them less suited for the application in large-scale physical model laboratories.

Alternative types of light sources have been applied in PIV measurements, such as Xenon lamps [7], flood lights for volumetric illumination [8], ambient sun light for large-scale PIV [9] and LED lights [10]. In the last two decades in particular, the application of LEDs for optical flow techniques has found increasingly interest [11,12], for planar PIV [13–17], micro-PIV [18–20] as well as in tomographic PIV (both in water [21,22] as in air [23]), volumetric particle tracking velocimetry [24] and particle shadow velocimetry [25]. Moreover, a line array of LEDs (a number of LEDs in a series circuit placed in line on a PCB) is able to provide high intensity illumination over a larger area of interest than using conventional laser illumination and encounter less shadowing of regions where the light is blocked by objects [13,16]. Furthermore, other than pulsed lasers used for PIV, LEDs do not require any pre-triggering providing very short rise times at very high repetition rates and the spatial and temporal (in between subsequent pulses) variation of the generated light pulses is negligible [14]. Developments in LED technology have led to an increase in the luminance, while reducing the costs and increasing lifespan [26]. LED light, other than laser light, is incoherent and uncollimated, making it less harmful to the human eye [26,27], such that less strict safety precautions are needed. On the other hand LEDs are not able to generate as intense radiation as class 4 pulsed lasers, demanding longer exposure time for sufficient illumination of tracer particles, which may lead to particle streaking or motion blur [28]. Additionally, the light sheet generated by LED arrays diverges much stronger than that of lasers, resulting in a variation of light sheet thickness throughout the field-of-view, which is considered as a source of PIV inaccuracies [29].

The application of such line arrays of LEDs as compared to class 4 pulsed lasers in PIV measurements in large measurement domains of physical hydraulic scale models is not investigated yet. Furthermore, the implications on safe application of LEDs as compared to lasers for PIV applications has not been assessed properly. Therefore, the goal of this

Fig. 1. Two examples of safety precautions that were taken at laser-based PIV measurements in the facility hall of Deltares to prevent risk of eye- and/or skin damage from laser light exposure. Left: a large tent of laser-safe shielding material in one of the scale model basins; Right: a wave flume with its PIV measurement section, which is completely shielded with multiplex plating.

work is to determine the applicability and implications of deployment of an array of LEDs as a light source for planar PIV measurements in large-scale experimental hydraulic setups. The investigation focusses both on theoretical and practical advantages and disadvantages of LEDs as compared to laser-based illumination. The influence of motion blur on PIV analysis is investigated, both theoretically as experimentally. A safety-assessment is performed in which the safety risks are compared between the deployment of a class 4 pulsed laser and two types of LED arrays. Furthermore, the applicability of both pulsed and continuous LED-based illumination is tested for two experimental setups. The flow in the first configuration is strongly inhomogeneous with large accelerations and a wide range of flow velocities, while the second case is a stratified flow characterized by low flow velocities and a transient mixing layer.

2. LED versus laser

The light properties of LEDs and lasers differ significantly. Lasers generate coherent, collimated and monochromatic light, resulting in a narrow beam of high intensity light, with very low divergence, making it ideal for the application in planar PIV measurements, where a thin light sheet of constant thickness is desired. On the other hand, the very high radiant energy makes lasers capable of producing thermal burns to the human skin and eye, while this is very unlikely to occur for LED light exposure [30], for which the light emission generally – in the absence of collimating optics - is strongly diverging. This makes them less hazardous to apply in publicly accessible surroundings than laser-based illumination, but at the same time brings up the challenge of providing light sheet conditions suitable for large-scale 2D PIV applications. In this work these conditions are defined as a light sheet thickness in the order of the interrogation window size (which is roughly in the order of 10 mm, with a 4 megapixel camera, 32 pixel interrogation window size and a measurement area of 1×1 m^2) and a modest divergence angle of the light sheet thickness (such that the variation of the light sheet thickness throughout the measurement domain remains limited). This section of the work presents an analysis of the main differences of the light sheet conditions and the consequences of applying the two different illumination sources in PIV systems for large-scale hydraulic setups.

2.1. Implications of LED-based PIV measurements

The pulse width (τ_p) of a pulsed PIV laser is in the order of 10 ns [5], while the required level of radiant energy (Q_e) for large-scale planar PIV measurements (field of view (FOV) of 0.5×0.5 m^2) is in the order of 10 mJ [5]. This combination results in very high radiant flux ($\Phi_e = Q_e/\tau_P$) of 1000 kW. Although LEDs are known for their overdriving capabilities (resulting in much higher radiations in pulsed mode than in continuous operation) [14] they are incapable of generating radiation levels as high as class 4 PIV lasers [26]. Hence, longer exposure times or pulse widths are demanded to obtain sufficient illumination for LED application in PIV measurements. However, for relatively long pulse widths, moving particles can displace significantly (as compared to the particle size) during illumination or exposure, which may result in a phenomenon known as *image blur* [3] or motion blur. The radiant energy that is received by a fast-moving particle during illumination, is distributed over a larger area than is the case for a slow-moving particle. The particle is therefore imaged over a larger area on the sensor array (CCD/CMOS). This blurring or *smearing out* of imaged particles (resulting in an asymmetric particle scattering intensity profile) can induce significant errors in time-resolved PIV analysis [28,31,32]. For example due to decrease in signal-to-noise

ratio, correlation peak skewing and other effects such as the assumption that the peak is rotationally symmetric in certain sub-pixel displacement estimators. Additionally, motion blur has shown to significantly increase the number of outliers in vector validation [28].

To characterize the effect of motion blur on the quality of an LED-based PIV (LEDPIV) measurement, the motion blur parameter (β_{mb}) is introduced in this work, defined as: $\beta_{mb} = (d_\tau + l_l)/d_\tau$, in which d_τ is the particle image diameter (as is introduced and defined in Ref. [5]) and l_l is the additional illuminated particle image length. This concept is graphically explained in Fig. 2. For a particle moving with a velocity u_p,

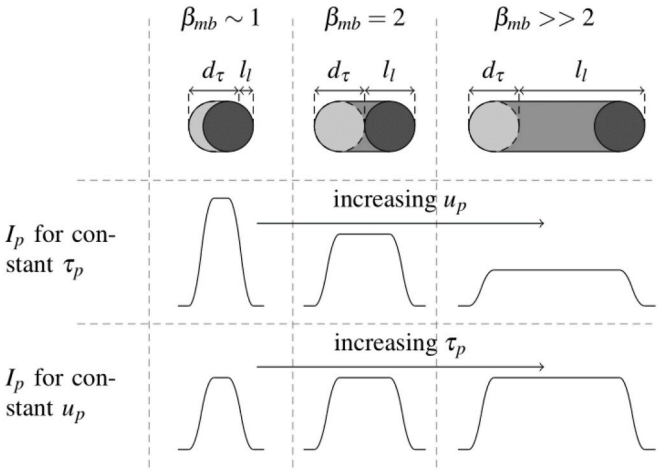

Fig. 2. Schematic representation of relation between pulse width τ_p and particle velocity u_p and influence of these characteristics on image blur parameter β_{mb} and radiant exposure of the imaged particle I_p (grey counts). The top row of the figure shows the illuminated path of a moving particle for three different values of β_{mb}, where the light grey and dark grey areas represent the start and end position of the imaged particle respectively and the grey part in between shows the trajectory of the imaged particle during illumination.

illuminated during τ_p, the illuminated image length can be estimated by: $l_l = M_0 u_p \tau_p$, where M_0 is the lateral magnification of the optical system (for a 1× 1 m^2 PIV plane and a 1 inch-type camera sensor, M_0 is in the order of 0.01). PIV measurements in which a double pulsed class 4 laser is used for illumination are represented by a value of β_{mb} close to unity, since τ_p (and thereby the value of l_l) is very small. The intensity of the particle image (i.e. the amount of reflected radiant energy distributed over the surface of the particle image, denoted by I_p in Fig. 2) scales inversely proportional to the imaged particle length (sum of d_τ and l_l), since the width of the imaged particle is not affected by image blur [28]. So, a fast-moving particle that is illuminated over a long period appears as a relatively low-intensity area, as can be observed in the intensity profiles sketched in the second row of Fig. 2 (corresponding to the case in which τ_p is kept constant and u_p is increasing). This type of motion blur decreases the signal-to-noise ratio of a PIV image, which increases the cross-correlation uncertainty in the PIV analysis [31]. Furthermore, when the illuminated particle length (l_l) is larger than the particle image diameter (corresponding to $\beta_{mb} > 2$), the intensity of the particle image will no longer increase since the illumination is distributed over a large area (as can be observed in the intensity profiles sketched in the bottom row of Fig. 2). Furthermore, it is expected that the quality of PIV images (i.e. images that provide a reliable application of correlation method to yield instantaneous velocity vector fields) is not improved in case $\beta_{mb} >$ 2 and will actually decrease with an increase in motion blur [28].

In Fig. 3 the influence of pulse width and particle velocity on motion blur is shown for three PIV setups of different dimensions (represented by a changing value of the field of view (FOV)), for a varying range of exposure time and flow conditions. Note that for the three cases the ratio between the particle image diameter and pixel size is in the order of 1.5–2.0, which has been shown as the optimal range to obtain reliable PIV measurements [3]. Image blur can be prevented by decreasing pulse widths, as can be observed in Fig. 3 where the region that corresponds to insignificant image blur (represented by small values of β_{mb}) lies at the left-hand side of the field associated with short pulse widths. Similarly, experimental conditions with small flow velocities correspond to small values of the motion blur parameter as expected. Somewhat less intuitive is the relation between motion blur and the measurement area (imaged with the same camera). Increasing the dimensions of the field-of-view reduces the motion blur parameter as can be observed from the lines displayed in Fig. 3. For example, in the case $u_p = 1$ m/s, the pulse width corresponding to $\beta_{mb} = 2.0$ increases from $\tau_p = 140\ \mu$ s for a small FOV of 0.15 m (dashed line) to 370μs and 1500 μs for FOV's of 0.5 m (dot-dashed line) and 2.0 m (solid line) respectively.

In addition to the relatively low irradiance, a challenge of LED-based illumination for PIV is strong divergence of the emitted light, due to its uncollimated and incoherent character. A varying light sheet thickness through the measurement domain will result in inhomogeneous light conditions, which negatively impacts the overall accuracy of PIV measurements [29]. Divergence of the LED bundle can be reduced by applying secondary optics, better known as collimators [33] to reshape the emission pattern of an LED into a narrow line light. Combining the right type of LED (small radiating surface and high luminous efficacy) with an appropriate collimator, forms a highly asymmetric elliptical LED beam [34]. A large array of these collimated LEDs positioned in line form a thin light sheet. Although collimated, the incoherent character of the LED light will result in significantly stronger divergence of the sheet thickness than is the case for a laser-based system. However, for relatively small distances from the LED source (or collimator), the light sheet is sufficiently thin providing suitable light conditions for planar PIV measurements (see Fig. 4).

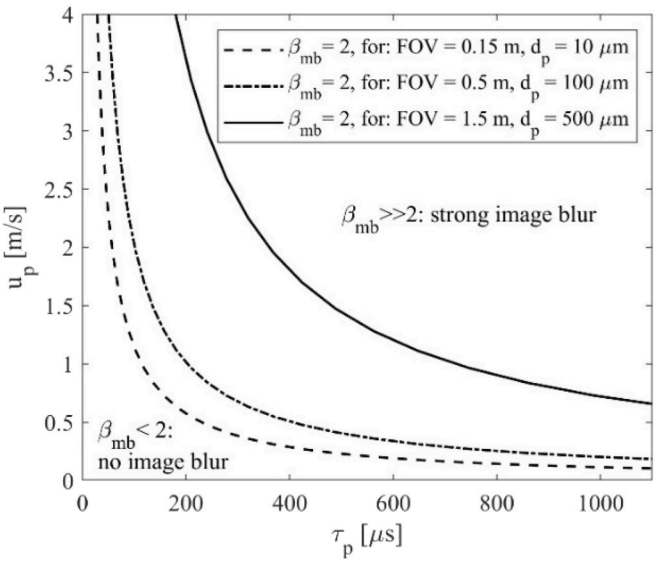

Fig. 3. Analysis of relation between pulse width (τ_p) and particle velocity (u_p in m/s) for a range of motion blur parameter values (β_{mb}) for three PIV setups with different values of the field of view (FOV), a 2000 × 2000 pix^2 camera with a 1-inch sensor. Conditions that correspond to a location at the right-hand side of each plotted line indicate a situation where image blur is to be expected.

2.2. Light sheet properties

Measurements were conducted to determine the light sheet properties of three different light sources: 1) pulsed class 4 Nd:YAG PIV laser (Litron Nano L 50–100 PIV, λ = 532 nm); 2) pulsed LED line light (DrewLear VLX2, 500 mm array, consisting of approximately 50 LEDs, equipped with a custom made cylindrical plano-concave lens to increase the light bundle's focal distance and the pulse width is set at $\tau_p = 200\ \mu$ s, λ_{peak} = 532 nm); 3) a commercially available continuous LED line array (where each of the 30 LEDs is equipped with a bundle collimator and a wide spectrum with 450 nm < λ < 750 nm, additional light source characteristics are given in Table 1). The (local) light sheet thickness (z_p) and light sheet length (y_p) are derived from imaged reflections of the light sources (see Fig. 5).

A set up is built consisting of a light source, located at a distance x_s from a white diffuse target, tilted 45° with respect to the horizontal axis (see Fig. 5). The side-scattered radiation is imaged by a camera (LaVision Imager MX 4M, equipped with a 28 mm Nikon Nikkor objective, $f^\# = 4.0$) positioned above the target, from which the distribution of the intensity of the light sheet at the target is derived (similar to the procedure introduced in Ref. [35] for estimating the light sheet thickness of a laser sheet).Fig. 6

From the full frame image, a rectangular region which covers the light sheet reflections is cropped, from which the intensity map is averaged along the width of 32-pixel rows (corresponding to a commonly chosen interrogation window size). This results in a large number of intensity distributions along the length (y-direction) of the imaged light sheet's reflections. At a specific y-location the light sheet thickness ($z_{p,s}(y)$) is obtained, which is defined as the full width half maximum (FWHM) of such a distribution. The maximum imaged intensity at the target (I_p) (which is proportional to the radiant exposure (H_e)) is defined as the maximum grey count value along the center (with respect to the length of the light sheet) intensity distribution.

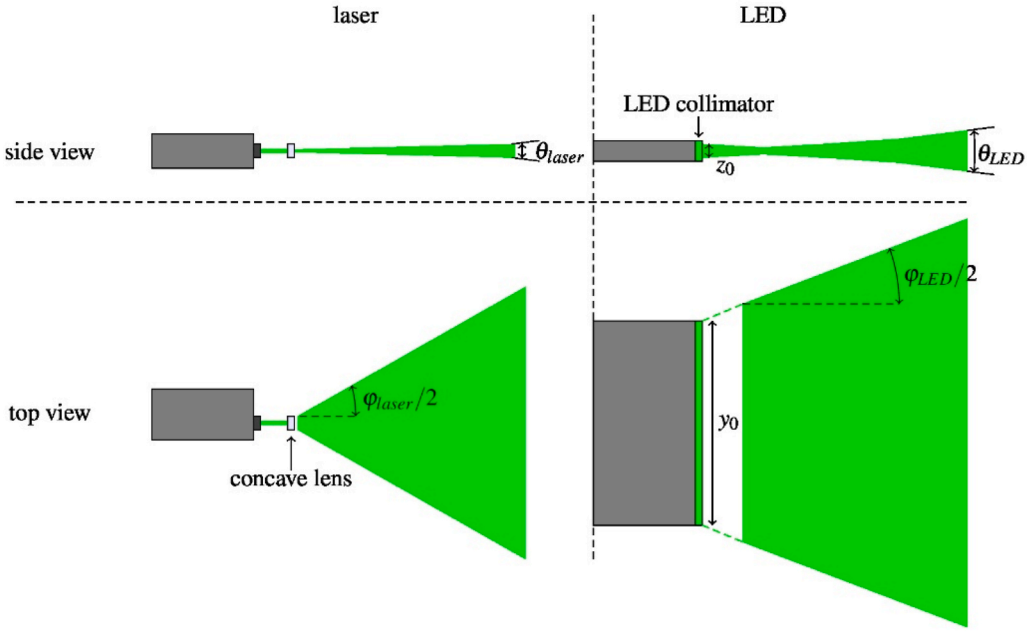

Fig. 4. Sketch showing similarities and differences between laser-based (left) and (collimated) LED-based (right) illumination for PIV measurements. The top view (top) and side view (bottom) sketches show the propagation of light sheet thickness and width respectively with increasing distance from the light source. θ and φ are the divergence angles of the (laser/LED) light sheet thickness and width respectively and z_0 and y_0 are the initial LED light sheet thickness and width.

Table 1
Properties of different light sources to analyze safety hazards, where Q_e is the laser's radiant energy, Φ_v is the LED's luminous flux, τ_p and f_p are the pulse width and repetition rate of the pulsed light sources respectively, θ, φ, z_0 and y_0 are expressed in Fig. 4. *this value is based on the "far field" ($x_s > 4.0$ m) divergence angle. ** due to the additional cylindrical lens to collimate the light bundle of the pulsed LED the total luminous flux is expected to be significantly lower (a conservative estimate of 90 % loss of luminosity is assumed) than the value obtained from the manufacturer's datasheet. ***this is a conservative estimation, based on visual observations during the measurements to determine the light sheet conditions.

Light source	Radiant energy (laser)/luminous flux (LED)	λ_{peak} [nm]	τ_p [s]	f_p [Hz]	θ [mrad]	φ [deg]	z_o [mm]	y_0 [mm]
Pulsed class 4 PIV laser	$Q_e = 50$ mJ (per pulse)	532	8e-9	100	1.2*	10.0	4	4
Pulsed LED (50 LEDS linear array)	$\Phi_v = 2730$ lm**	532	200e-6	100	34	43.0	20	500
Continuous LED (30 LEDs linear array)	$\Phi_v = 14{,}900$ lm	n/a (wide spectrum 450–750)	–	–	92	10.0***	20	750

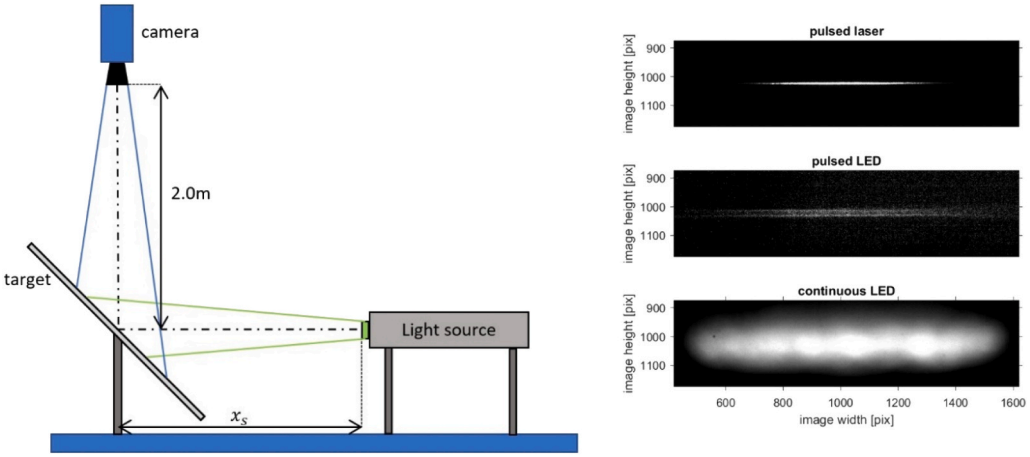

Fig. 5. Measurements of light sheet properties of the studied light sources. Left: sketch of set up with diverging light sheet reflecting on target and imaged by the camera. Right: imaged intensity map of the three light sources for $x_s = 0.5$ m. The intensity of the continuous LED seems much higher than that of the pulsed LED due to the longer exposure duration (complete exposure time of image = 26 ms), while the pulsed LED exposure duration is only a fraction of that ($\tau_p = 200\ \mu$ s).

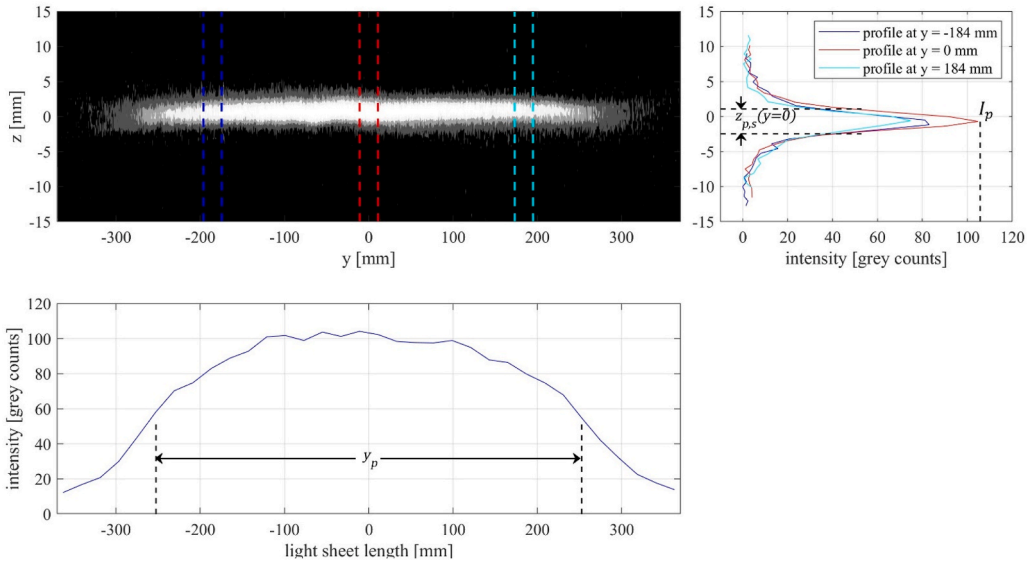

Fig. 6. Light sheet properties obtained from the image of the reflected light bundle of the pulsed LED at $x_s = 0.25$ m. Top left: cropped raw image showing intensity map of light bundle; Top right: distributions of averaged intensities across the width of the three outlined areas in the top left subfigure, with z_p indicating the light sheet thickness based on the FWHM of the intensity profile along the center of the image and I_p the maximum intensity value of this profile; Bottom: distribution of the maximum intensity values along the length of the light sheet, with y_p the light sheet length.

Furthermore, the length of the light sheet y_p is defined as the FWHM of the distribution of these maxima. The mean light sheet thickness z_p is defined as the mean of all the light sheet thickness values along y_p (all values of $z_{p,s}$).

The results of these measurements are shown in Fig. 7 and Table 1. For values of x_s larger than 1.0 m and 2.0 m of the reflected pulsed LED and continuous LED bundles respectively, the imaged intensities were so small that the image processing did not give accurate results for these cases, therefore these results are not presented. Furthermore, to prevent oversaturation of the CMOS sensor, the camera was equipped with a double neutral-density filter (Hoya HMC-ND8) for the measurements with the pulsed laser. A reduction factor was obtained by measuring the intensities of two identical light sheet reflections with and without the double neutral density filter. Note that, although the plane of the target at which the light sheet is reflecting is not parallel with the image plane, for relatively thin light sheets, linear mapping of image coordinates (pixels) to world coordinates (meters) gives sufficiently accurate results.

As can be observed in Fig. 7 the light sheet characteristics of the three different light sources strongly vary. It should be noted the vertical axes of the top and bottom subfigures are logarithmic. The light sheet thickness of the pulsed laser hardly changes with x_s, while both the pulsed and continuous LED sheet thicknesses increase significantly. This is expected and corresponds to the main difference between collimated and coherent laser light and diverging and incoherent LED bundles. The light sheet lengths on the other hand show a less clear trend. The light sheet length of the pulsed laser and pulsed LED increases with a factor 1.5 to 2 respectively for 0.25 m $< x_s <$ 0.75 m, while the light sheet length of the continuous LED shows a slight decrease, which is not as expected. A decrease of the light sheet length with increasing distance to the source would, for a sufficiently large value of x_s result in a very narrow light sheet, which was not observed during the tests. Therefore, it is assumed that the definition of the light sheet width as the FWHM of the intensity distributions along the y-direction is not applicable for the intensity map of the continuous LED. A conservative estimate of a constant light sheet length for the continuous LED is therefore proposed. The divergence angle of the light sheet thickness and length for all values of x_s are obtained using ordinary trigonometry. These values are averaged over all values of x_s and listed in Fig. 7.

The maximum intensity values all strongly decrease with increasing values of x_s as expected and the significant difference in intensity peak between the pulsed laser and pulsed LED is striking. The intensity of the continuous LED is, other than expected, much larger than that of the pulsed LED, even though the latter is (slightly) overdriven. This is expected to be caused by the relatively large exposure time of the camera. While, in case of the pulsed LED, the camera's sensor is illuminated for a duration equal to the pulse width (=200 μ s) of the pulsed LED, the sensor is illuminated during the complete exposure time (26.4 ms) for the continuous LED.

2.3. Safe working conditions

To assure safe working conditions, the exposure of human eye and skin to laser or LED light should remain below a defined maximum permissible exposure (MPE). In appendix A, a safety analysis is performed in which eye and skin safety hazards are compared for a person working in the vicinity of the light sources as investigated in section 2.2: a pulsed class 4 PIV laser, a pulsed LED and a continuous LED. The properties of the different light sources are given in Table 1. From the safety analysis it is concluded that the LEDs considered, can be used in an eye- and skin-safe way without having to apply any safety regulations, thereby reducing preparation time and costs of an experimental campaign in which a PIV setup is used. In case a class 4 laser is applied, strict safety precautions have to be met to prevent exposure to both the eye and skin, even for exposure to reflections from extended sources.

3. Results: LED-based PIV measurements

For two experimental setups the performance and applicability of LEDs as light source for PIV measurements are described. Both tests are conducted in the hydraulic facility hall at Deltares, Delft, the Netherlands. The LEDPIV results are compared with data from conventional measurement methods (i.e. pitot tube measurements and

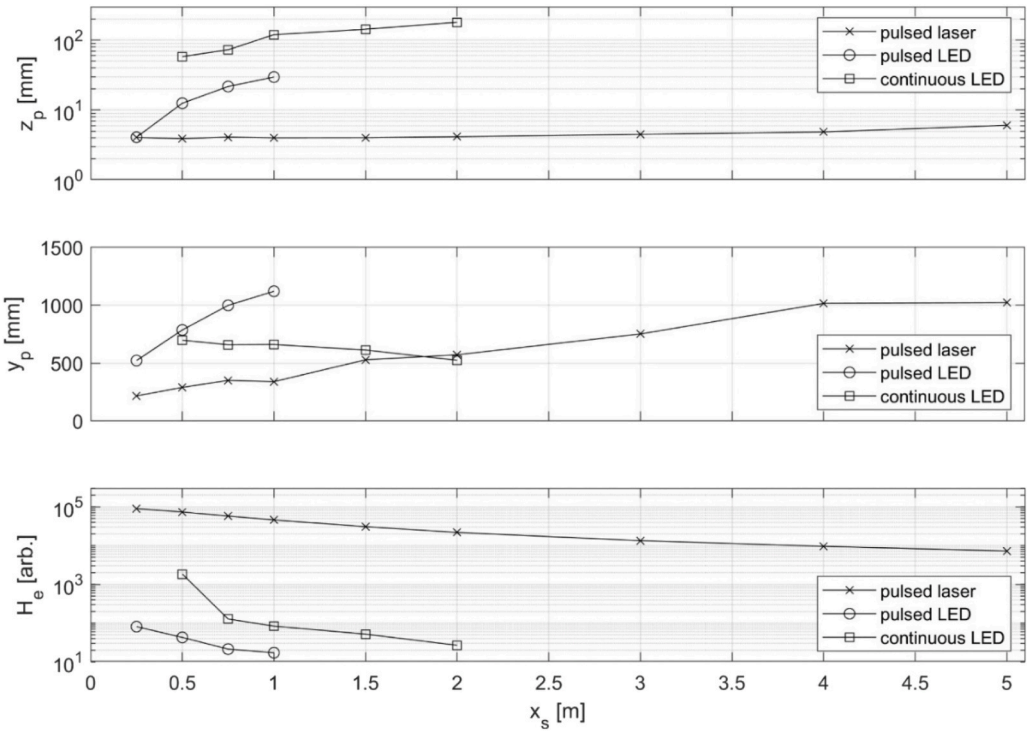

Fig. 7. Variation of light sheet properties (z_p is light sheet thickness, y_p is light sheet length and I_p is the maximum intensity value) with distance from the light source (x_s) for the three different illumination sources. The intensities of the pulsed LED for $x_s > 1.0$ were so small that the light sheet characteristics could not be obtained and therefore no data is plotted for these values. The same yields for $x_s > 2.0$ m for the continuous LED.

laser-based PIV measurements). The first test-case is a converging, relatively high-speed accelerating flow into and through a bell mouth, while the latter case comprises a stratified flow in a large measurement domain, with relatively low velocities. Note that in the first case a pulsed LED array is used as illumination source, while for the second case both PIV measurements are conducted with a conventional pulsed laser and a continuous LED array.

3.1. *The flow in and around a bell mouth of a vertically submersible pump*

Obtaining the characteristics of the flow in pump sumps is of great interest since this can significantly improve the performance and efficiency of such a system [36]. Typically, applications are in cooling water intake pumps or waste-water pumping stations. In addition to mean flow characteristics, it's desirable to quantify unsteady flow phenomena, such as free-surface and wall-attached vortices. This is done through controlled physical scale model tests as prescribed by the ANSI/HI 9.8 standard [37], where flow quantification is conventionally obtained with pitot tube measurements and rotation meters [38,39], in combination with a qualitative analysis using dye injection. These instruments are intrusive and only provide pointwise information of the flow. 2D PIV measurements on the other hand are non-intrusive and characterize the flow in a plane at high spatial resolution.

LED-based PIV measurements are conducted in a scale-model setup of a pump sump, which is built in the intake- and outfall structure (IOS) basin, which is located in the hydraulic facility hall at Deltares [13]. The bell mouth has an internal diameter of 200 mm with a smooth curvature, which is connected to a suction pipe with a diameter of 110 mm. The throat of the suction pipe is located at 55 mm from the bell mouth entrance. The pump discharge is varied, while the still water level is 800 mm for all conditions and the bottom clearance of the pump is 80 mm. Application of a pulsed laser in such a basin would require shielding of large parts of the basin, which is time consuming and labor-intensive, making it a suitable test-case to apply a pulsed LED. The setup consists of a commercially available pulsed LED line light (DrewLear VLX2, equipped with a custom-made lens, characteristics as listed in Table 1) as light source. In pulsed mode the LEDs are overdriven to 40 % above the maximum continuous level of operation. A bi-convex lens (with radius of curvature $r = 135$ mm) is positioned in front of the LED line array to collimate the light bundle, which provides a light sheet thickness of 4–10 mm (see Fig. 7) within 0.5 m from the LED collimator. The compartment where the suction pipe is located is equipped with a transparent false bottom. A tilted mirror reflects the light sheet such that it is oriented vertically, providing illumination throughout the vertical center plane below and inside the transparent bell mouth (size of measurement plane is approximately 0.3×0.3 m^2) as can be observed in the right-hand side of Fig. 8.

LED-based PIV measurements are conducted for five different discharge levels Q (5–35 l/s, as listed in Table 2), corresponding to a mean vertical velocity in the suction pipe of $w_{pipe}\left(= Q/\pi(D_i/2)^2 \right.$, where D_i (=110 mm) is the internal diameter of the suction pipe), ranging from 0.5 to 3.7 m/s. The flow is seeded by a grid of small nozzles at the upstream end of the comportment that dispenses a highly concentrated mixture of water and 100 μ m polyamide spheres (Vestosint 1101, $\rho_s =$ 1060 kg/m^3) acting as tracer particles. The reflections of the particles are imaged with a CCD sensor (LaVision Imager Pro X 4M) equipped with a 28 mm Nikon objective ($f^{\#} = 4.0$). To prevent ambient light influencing the light conditions, the surrounding of the setup is partially covered with shielding material. Image acquisition and pre- and post-processing of the images is performed with the software of LaVision (Davis 8.3.1). A total of 12 different data sets are obtained (see Table 2), each consisting of a 500 frame pairs (except for the 15b, 15c and 15d cases, which consist of 100 frame pairs only), acquired at 4.1 frame pairs per second. Background subtraction (in which the background is defined as the time-average of the raw images of each complete dataset) is applied prior to performing spatial cross-correlation. Due to low seeding concentration, interrogation window size is relatively high and set to $D_I^2 = 128 \times 128$ pixel^2 (providing reasonable time-averaged values for the number of imaged particles per interrogation window), with a 75 %

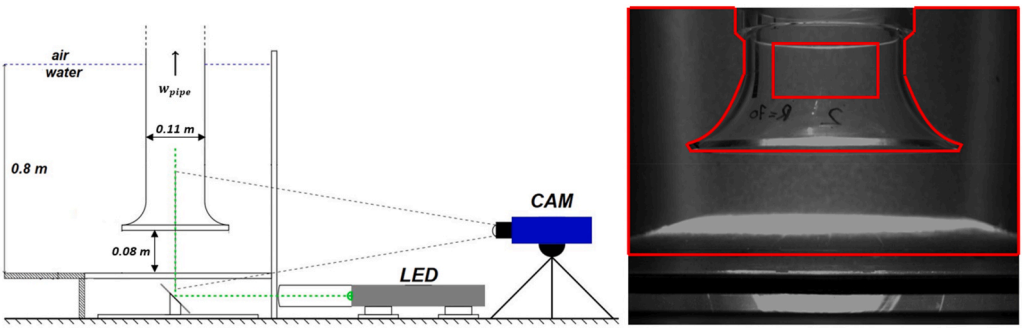

Fig. 8. Setup of LEDPIV measurement of a pump sump scale model. Left: Schematic side view, with the pulsed LED line light positioned below the camera and a mirror below a transparent false bottom. Right: field-of-view from the camera of the transparent bell mouth, with red outlined the region in which the PIV analysis is performed.

Table 2
Experimental conditions for the first test-case, where ΔX_p is the in-plane particle displacement in an interrogation window, given as a ratio of the interrogation window size, with d_r is the pixel distance of the camera sensor. *motion blur parameter based on illuminated particle image length (l_l) estimated inside the suction pipe: $l_l = M_0 w_{pipe} \tau_p$. ** w_{avg} is the vertical flow velocity within the pipe at 58 mm above the bell mouth entrance averaged over its width (note that due to low seeding density and strong curvature of the transparent pipe no reliable measurements are obtained close to the pipe walls and therefore PIV data is only considered of the center 80 mm across the width of the suction pipe).

Case	Q (l/s)	w_{pipe} (m/s)	Δt (μs)	τ_p (μs)	ΔX_p (%)	β_{mb}* (−)	$\overline{w}_{avg}$** (m/s) (PIV)
5a	5	0.53	3000	150	8.7	1.5	0.51
15a	15	1.58	1500	150	13.0	2.6	1.50
15b	15	1.58	1500	260	13.0	3.8	1.50
15c	15	1.58	1500	440	13.0	5.8	1.50
15d	15	1.58	1500	750	13.0	9.2	1.48
25a	25	2.63	1250	200	18.1	4.6	2.49
25b	25	2.63	1500	300	21.7	6.4	2.47
25c	25	2.63	500	150	7.2	3.7	2.49
30a	30	3.16	700	175	12.2	4.8	2.99
30b	30	3.16	500	250	8.7	6.4	2.99
35a	35	3.68	450	150	9.1	4.8	3.49
35b	35	3.68	400	200	8.1	6.1	3.46

overlap this results in a velocity vector spacing of 4.5 mm/vector. Additionally, providing sufficient seeding close to the bell mouth walls was found to be challenging. Therefore, velocity data is only obtained within the area covering 80 mm along the width of the center of the suction pipe. Universal outlier detection [40] is applied for vector validation.

For the 25 l/s discharge case the LEDPIV results are compared with pitot tube measurements [38]. To investigate the applicability of the pulsed LED line light, varying values of the pulse width are chosen for different discharge levels.

3.1.1. Quality of LED-based PIV data

During preparations of the measurements, the minimum pulse width of the LED to enable sufficient illumination of the seeding particles was found to be $\tau_p = 150$ µs. For larger pulse widths at moderate to high flow rates, image blur of the particles is observed (represented by large values of the image blur parameter β_{mb}), as is shown in Fig. 9.

To investigate whether image blur influences the accuracy and reliability of the PIV measurements, the percentage of first choice vectors (displacement vector is based on first correlation peak) is obtained for the different measurement conditions. The average of the percentage first choice vectors of the first 100 instantaneous vector fields is found to be sufficiently high (larger or equal to 95 % [13]) for all measurement conditions. Note that this high percentage is based on the complete measurement area, where most of the field-of-view lies outside the suction pipe and therefore is represented by low flow velocities, where image blur is limited. To investigate the influence of image blur on the PIV analysis, only the image data that covers the area inside the suction pipe is considered (i.e. the area from 35 mm up to 77 mm above the bell mouth entrance and the center 80 mm across the width of the suction pipe).

From analysis of the measurement data no apparent correlation between the particle displacement (ΔX_p) and the number of obtained first choice vectors is obtained. This is as expected, since the experimental conditions were such that the four PIV design rules (as stated in equation (8.88) in Ref. [5]) are all fulfilled, assuring a sufficiently high image density, limited loss of in- and out-of-plane particle displacement and small spatial gradients within the interrogation domains.

3.1.2. Flow characterization with LED-based PIV

Time-averaged velocity profiles of the vertical velocity component are obtained along the width of the suction pipe at the throat (which is located 55 mm above the bell mouth entrance (see Fig. 10). The time-averaged data is based on 500 vector fields, except for cases 15b, 15c and 15d, for which only 100 frame pairs were obtained.

In Fig. 10 the measured velocity profiles are shown for different cases and for one case at different values of the motion blur parameter. As can be observed in the left-hand side of Fig. 10, the shape of the vertical velocity profiles is reasonably similar for the different discharge cases. The time-averaged values are normalized by dividing it with the mean bulk velocity in the suction pipe (w_{pipe}). The maximum flow velocities range between 0.5 m/s and 3.5 m/s for the 5 l/s and 35 l/s discharge cases respectively. For each discharge level, the case with the lowest corresponding motion blur parameter is plotted. As can be observed, the velocity profiles are notably different from conventional non-accelerating pipe flow, with the minimum flow velocities at the center and the maxima close to the pipe wall. This corresponds to the shape typically observed in the suction pipe of a vertically submersible pump [38]. The results for the four different experimental conditions of the 15 l/s discharge case (right-hand side of Fig. 10) seem to overlap reasonably. However, the magnitudes of the time-averaged vertical velocity component seem to decrease with an increase in LED pulse width (or, equivalently the motion blur parameter β_{mb}). The velocity profile corresponding to case 15d consequently lies below the data corresponding to case 15a (except for the data at $x \sim$-40 mm). Spatially averaging the values of the velocity profile along the width of the suction pipe gives the mean vertical velocity $\overline{w}_{avg}$.

The values of $\overline{w}_{avg}$ for cases 15a-15d are listed in the legend of the right-hand side of Fig. 10. These values consistently decrease with an increase of β_{mb}, which is in accordance to previously performed PIV analysis of a synthetic jet affected by motion blur [28] that show a decrease in measured velocities between in-focus and blurred PIV data. This "motion-blur effect" appears to have similarities with the known bias in PIV results for mean velocities towards 2 % lower velocities, due

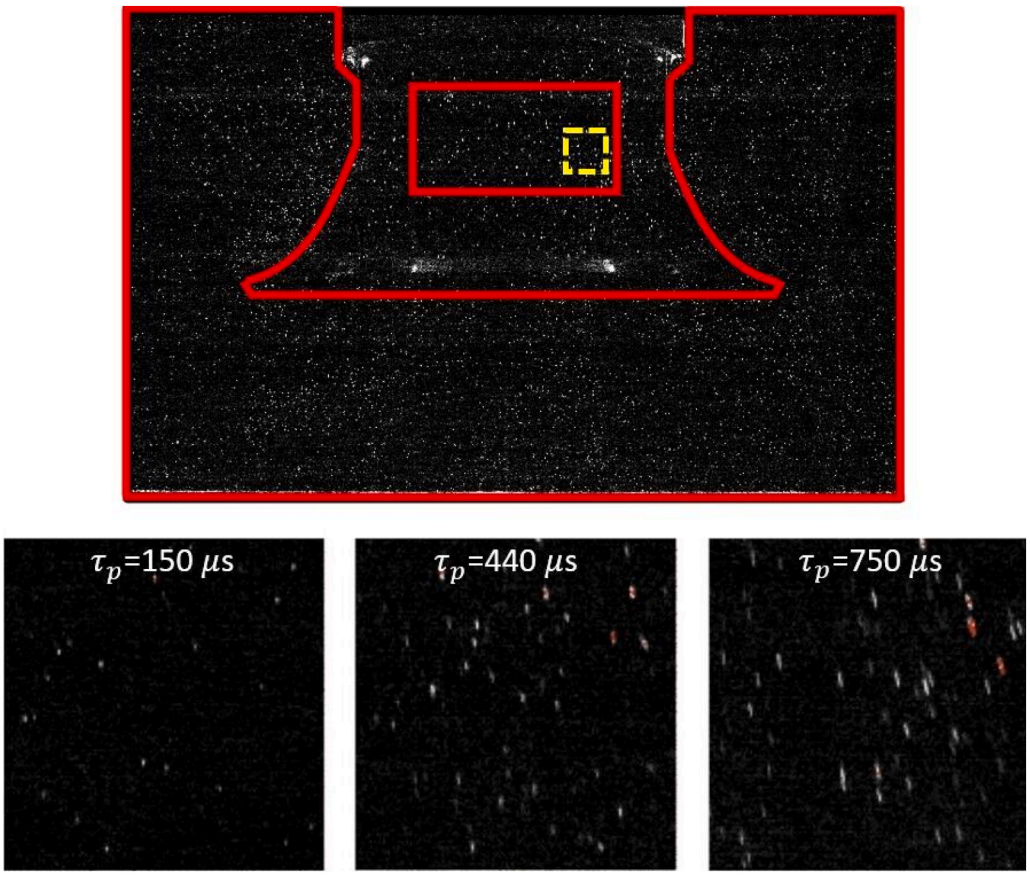

Fig. 9. Raw images as obtained in the pump sump setup. Top: instantaneous image of the field-of-view for case 15c, with red contour denoting the masked area and the yellow-colored rectangle indicating the area as shown in the three bottom subfigures. Bottom: Example of image blur for increasing exposure time of the flow within the bell mouth at constant discharge ($Q = 15$ l/s). Left: $\tau_p = 150$ µs, $\beta_{mb} = 2.6$, center: $\tau_p = 440$ µs, $\beta_{mb} = 5.7$ right: $\tau_p = 750$ µs, $\beta_{mb} = 9.0$.

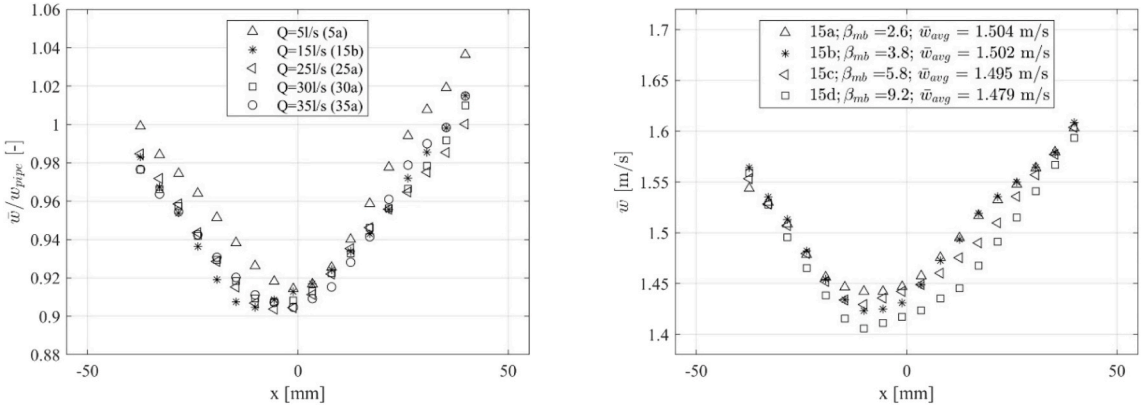

Fig. 10. Time-averaged, velocity profiles of the vertical velocity component at 58 mm above the bell mouth entrance for different discharge levels over the width of the suction pipe (internal diameter = 110 mm), at 58 mm above the bell mouth entrance. Left: normalized velocity profiles for the different discharge levels; Right: absolute velocity profiles for $Q = 15$ l/for varying pulse widths, 15a = 150µs, 15b = 260µs, 15c = 440µs, 15d = 750µs.

to 'fast' tracer particles leaving the interrogation area [5].

A similar relation between motion blur and the PIV-based velocities is observed in the left-hand side of Fig. 11. This subfigure shows the relation between the motion blur parameter (β_{mb}) and the vertical velocity within the suction pipe from the LED-based PIV measurements. The values shown are the magnitude of the time- and spatially (across the width of the suction pipe at 58 mm above the bell mouth entrance) averaged vertical velocity ($\overline{w}_{avg}$) for all measurement conditions (normalized by the bulk velocity w_{pipe}) as a function of the corresponding motion blur parameter. The inversely proportional relation between motion blur and the PIV-based velocity is also clearly visible from the negatively oriented linear polynomial fit. A PIV measurement with a corresponding motion blur parameter of $\beta_{mb} = 9$ results in a 2 % lower velocity magnitude as compared to a PIV measurement for which $\beta_{mb} = 2$. For the PIV-based velocities obtained at different heights throughout the suction pipe (velocity profiles are obtained up to 77 mm above the bell mouth entrance) this negative relation is observed for all datasets. In case the motion blur parameter is based on the measured mean flow velocity $\overline{w}_{avg}$ instead of the bulk velocity w_{pipe} (such that the illuminated particle image length is: $l_l = M_0 \overline{w}_{avg} \tau_p$) a similar relation is observed.

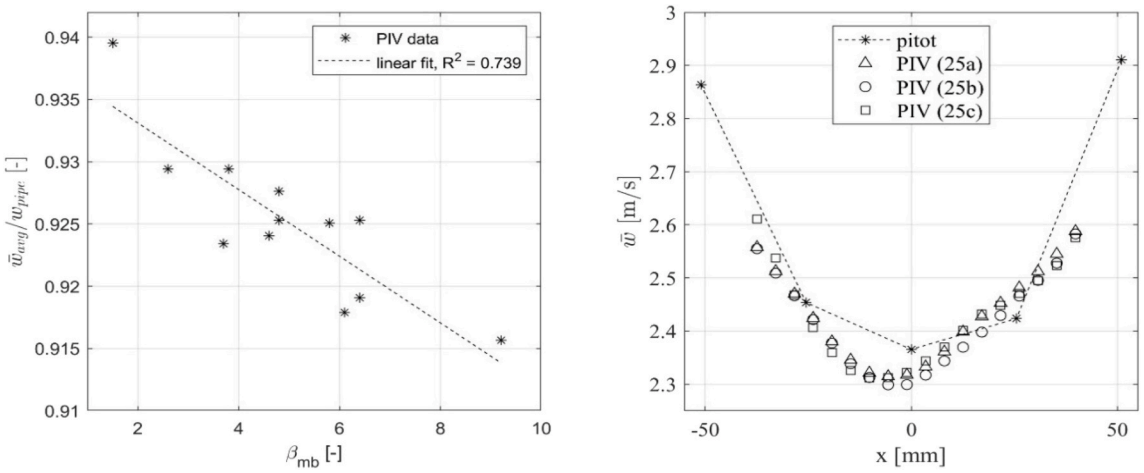

Fig. 11. Left: relation between motion blur parameter (β_{mb}) and the temporally and spatially averaged vertical velocity within the suction pipe (at 58 mm above the bell mouth entrance). Right: Time-averaged velocity profile at the throat of the vertically submersible pump (58 mm above the bell mouth entrance) for the 25 l/s discharge cases ($\beta_{mb} = 4.6$ (25a); $\beta_{mb} = 6.4$ (25a); $\beta_{mb} = 3.7$ (25c)), compared to pitot tube measurements (measured at 55 mm above the bell mouth entrance). Note that the setup of the pitot-tube measurements is equipped with a cone at the bottom below the bell mouth to avoid the generation of submerged vortices and thereby slightly differs from the PIV setup.

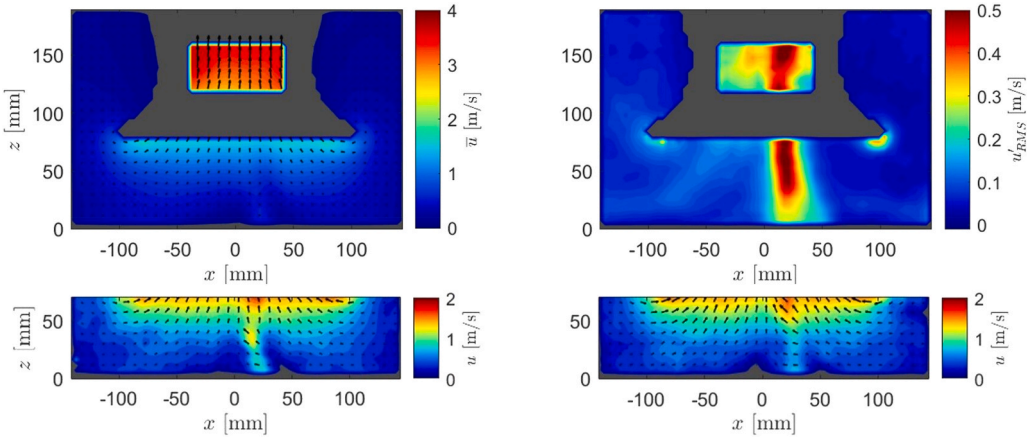

Fig. 12. Top: Time averaged vector field (top left) and root-mean-square values of the fluctuations (top right) of the flow in and around the bell mouth for a discharge of 35 l/s. The grey region is masked in the analysis since it is blocked visually by the strongly curved bell mouth. Bottom: Two subsequent instantaneous velocity fields of the subregion below the bell mouth, showing the influence of the submerged (bottom-attached) line vortex on the flow field. Note that the vector scaling differs between the top and bottom subplots. For clarity, every 2nd velocity vector is plotted in the top left and bottom figures.

The vector fields of the time-averaged and root-mean-square (RMS) of the velocity variations for the 35 l/s discharge (35a) case are shown in the top panels of Fig. 12. The flow velocities are small outside the bell mouth and show a strong increase inside the contraction towards the suction pipe. To determine the time-averaged values, it is imposed that at each vector location, at least half of the total sequence of instantaneous LED-based PIV data should contain a valid vector to obtain an average. The time-averaged vector field is symmetric throughout the measurement area, except for a thin region of increased velocity magnitude, which is located on the right-hand side below the center of the bell mouth. The vector field of the RMS velocity fluctuations shows a prominent region of high velocity fluctuations below and inside the bell mouth just right from the center below the bell mouth entrance. This is an indication of the presence of a submerged vortex that is formed at the bottom [38]. Such vortices are commonly observed in full-scale and scale models of pump sumps [41] and occur between the suction pipe and the bottom floor below the bell mouth as well as between the suction pipe and the side- or back walls around the bell. The formation of such submerged vortices strongly relates to the swirl (i.e. non-uniformity) of the approach flow, which depends on the geometry of the approach flow setup and its flow properties. The geometry of the channel upstream of the bell mouth which is used in the testcase contains a bend and thereby an asymmetric approach flow and the associated asymmetric submerged vortex is induced. For a complete description of the setup the reader is referred to Ref. [13]. Since the line vortex' position is dynamic (its center and the fluid rotating around it are moving in time), the velocity fluctuations of the Eulerian flow field as obtained from the PIV analysis (right hand side of Fig. 12) show a strong and distinct peak in the region where the line vortex occurs. From inspection of the raw images, a variation to the mean motion of the particles is observed through this region. Particles are being swept chaotically from left to right, or from right to left (as can be observed from the instantaneous velocity fields shown in the bottom subfigures of Fig. 12), while the mean direction of the flow is upwards, indicating the presence of a submerged vortex. A less intense region of higher RMS fluctuations is observed in the left side region below the bell mouth entrance, starting at the left side wall, indicating a wall vortex commonly witnessed in physical scale model tests of pump sumps. It should be noted that the main point of the top right panel of Fig. 12 is to show that the presence of a submerged line vortex can be readily identified via inspection of the RMS field of the

velocity fluctuations rather than describing the statistical characteristics of the submerged vortex. Identifying the presence and intensity of such vortices is one of the most relevant issues to investigate in bell mouth tests like these for which conventionally dye injection is applied [41]. Inspection of the RMS field of the velocity fluctuations could be a non-intrusive and more objective alternative method for vortex detection. It is however not in the scope of this work to further investigate the applicability of such a vortex detection method.

3.1.3. Data comparison

For the 25 l/s discharge case, the LED-based PIV results are compared with pitot tube measurements [38] (see right-hand side Fig. 11). The results of the LEDPIV measurements at 58 mm above the bell mouth entrance (or 138 mm above the bottom of the pump sump compartment) fall within 3 percent of the velocities measured with the pitot tube (measured at 55 mm above the bell mouth entrance). The right-hand side of Fig. 11 also shows that the velocities from the LED-based PIV measurements are smaller than obtained from the pitot tube measurements. The underestimation is in the same order as the 2 % bias error known in PIV measurements as mentioned in the previous subsection. For the other discharge cases no comparison can be made, since pitot tube measurement data is only available for the 25 l/s discharge case. It should be noted that the setup in which the pitot tube measurements were performed slightly differs from the LEDPIV setup, since the former setup is equipped with a cone (diameter 150 mm, height 70 mm) which is placed below the bell mouth to avoid the generation of a submerged vortex from the pump sump bottom. The influence of the cone on the flow patterns is observed in the larger deviation between the pitot- and PIV measurements in the region on the right-hand side of the pipe's center (between $10 < x$ (mm) < 30). The flow in this region is strongly influenced by the submerged vortex, which is also observed in the velocity fluctuations field for the 35 l/s discharge case (shown in the right-hand side of Fig. 12). Despite this difference in setups, the magnitudes of the vertical velocity obtained with the two different measurement techniques show reasonable resemblance.

3.2. Selective withdrawal in a stratified flow

The second test-case is based on measurements performed in a scale-model that is set up in the Lock Facility at Deltares. In this scale model, the performance of a salt screen which will be placed in the discharge channel at the newly built sealock of IJmuiden is investigated. The salt screen reduces the intrusion of saltwater inland into the North Sea channel by applying the so-called *selective withdrawal* principle: the top part of the discharge channel is blocked, thereby withdrawing only the bottom part of the stratified flow at the channel side which contains mainly salt water [42]. As for the previous test-case with the vertically submersed suction pipe, application of a class 4 PIV laser in such a setup would demand shielding of a large part of the basin with laser shielding material to prevent unsafe conditions for people working in the vicinity of the setup (i.e. due to laser-related eye- and skin hazards).

The segment of the scale-model where the salt screen is located is made of Polymethyl methacrylate (PMMA) to enable optical access to the area of interest (see left-hand side of Fig. 13). The total discharge is 30 l/s and the waterdepth is approximately 0.58 m at the location of the salt screen. The line array of continuous LEDs (similar characteristics as the continous LED listed in Table 1) is positioned below the salt screen and oriented upwards to form a vertically oriented plane. In addition to the LED-based tests, additional PIV measurements are conducted with a double-pulsed Nd:YAG laser ($\lambda = 532$ nm, $Q_s = 50$ mJ/pulse), equipped with laser optics (two concave lenses and a mirror) to form a diverging light sheet (with characteristics as listed in Table 1, note that the diverging angles of the light sheets differ (i.e. get smaller) when radiating through an air-water interface) of similar dimensions as the region that is illuminated by the LED line light. The flow is seeded with 100 μ m polyamide spheres ($\rho_p = 1060$ kg/m^3) at the inflow of the model and the field-of-view is imaged by a CMOS camera (LaVision Imager MX 4M), with a 28 mm lens (Nikkon Nikor 28/f2.8, $f^{\#} = 5.6$), providing a field-of-view of approximatley 0.7×0.7 m^2 (for a full description of the setup the reader is referred to Ref. [42]).

Image acquisition and data processing are both performed with the software of LaVision (DaVis 8.4). The low flow velocities lead to a relatively large interframe time ($\Delta t = 26.3$ ms) and frame pairs are acquired at 1 Hz. The exposure time of each frame is set at 5 ms and the total acquisition time is 600 s, resulting in 600 image pairs. After image calibration and pre-processing (background subtraction), spatial cross-correlation is applied to each frame pair to obtain a displacement field. The interrogation window size of the second interrogation step is 32×32 pix^2 ($D_I = 64$ pix for first interrogation step), which with 50 % overlap results in a vector spacing of 5.4 mm.

3.2.1. Data comparison

The major difference between the laser-based and LED-based PIV measurements is the exposure time or pulse width of the illumination, which is six orders of magnitude larger for the continuous LED-based

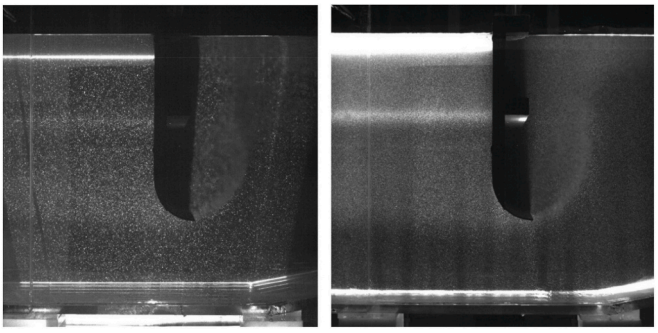

Fig. 14. Raw images of the seeded flow along the salt screen for (left) the laser-based and (right) the LED-based illumination.

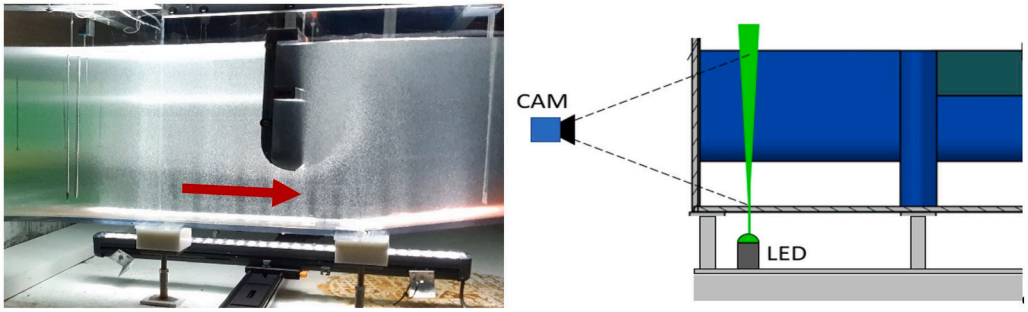

Fig. 13. Left: Picture of continuous LED line light and illuminated part of seeded stratified flow (in direction of the red arrow) in scale model of selective withdrawal project of the IJmuiden lock; Right: sketch of part of salt screen, as seen from the downstream side of the flow, with side-view of LED light sheet setup.

PIV (the pulse width of laser is 8 ns and exposure time of the camera for the continuous LED is 5 ms). The effects of this difference on the raw images are shown in Fig. 14. Due to the low flow velocities (up to 0.15 m/s), the effect of motion blur seems rather limited (with a motion blur parameter β_{mb} of approximately 2 for the regions with the highest flow velocities and β_{mb} ~1 for the low velocity, fresh water flow region), although the particles do not seem as clearly focused as for the laser-based case. The larger light sheet thickness of the LED (as can be observed in Fig. 7, the light sheet thickness of the continuous LED is approximately 10 cm at the free-surface) results in a thicker plane of illumination, such that the location of the imaged particles is less well-defined than for the laser-based case. This is observed in Fig. 14 as well, where the area at the free-surface where the LED reflects on is much larger than for the laser-based situation. Note that the depth of field of the optical setup is in the order of 0.5 m, such that the imaged particles within the LED sheet are considered in focus. A slight shadowing effect along both sides of the salt screen is observed for the situation with the laser. This is caused by spreading of the laser beam, resulting in an area that is not illuminated by the laser, which increases with distance from the light source. This is not the case for an array of LEDs, since it consists of a large number of light emitting sources. On the other hand this induces inhomogeneous light conditions, with individually observable bundles along the width of the field-of-view. The effect of these differences on the PIV results after preprocessing (i.e. background subtraction) is however found to be limited.

Note that for the laser-based experiments a large area around the measurement domain had to be shielded by a structure covered with laser-safe material to prevent laser light radiating to people present in the vicinity of the setup. For the LED-based case shielding the setup with laser-safe material is not necessary, since the calculations in section A1 show that the radiation levels of the continuous LED are non-hazardous for the human eye and skin. Note that in the LED-case, local shielding of only a smal part of the setup is needed to prevent ambient light negatively influencing the light conditions at the PIV measurement section.

As can be observed in Fig. 15, the time-averaged vector fields obtained from the PIV measurements with the two different illumination sources show similar characteristics of the flow around the salt screen. A strongly stratified streamwise oriented flow at the upstream part is observed, which is directed upwards downstream of the salt screen. A difference between the two PIV measurements can be observed at the bottom corners of the field-of-view, where a larger extend is being illuminated by the LED, while the limited expanding of the laser sheet results in two small regions without velocity vectors.

A quantitative comparison between the performance of the two light sources is shown in Fig. 16. For the upstream part of the flow (x <80 mm) the magnitudes of the flow velocities are closely overlapping (deviations are within 5 % of the magnitude of the laser-based measurements). Note that the maximum value of the corresponding motion blur parameter (assuming the highest flow velocities ~ 0.10 m/s) remains below 2.0 for these experimental conditions and therefore no influence of motion blur on the flow velocities from the LED-based PIV measurements is expected. Moving downstream along the salt screen, the differences between the profiles increases slightly. In the vicinity of the salt screen, the differences are still small, however, for the velocity profiles at $x = 80$ and $x = 150$ deviations are significant (i.e. 10-20 % of the laser-based velocities) for both the streamwise and the vertical component. It should be noted that performing PIV measurements throughout this region (from $x = 150$ mm and further downstream) is challenging due to mixing of the salt and fresh water layer, causing a variation in refractive index of the fluid and thereby resulting in distortion of the imaged particles (as is observed directly downstream of the salt screen in Fig. 14). In addition to that, the difference in light sheet thickness of the laser and LED influences the PIV results in the downstream part of the flow. Other than the predominantly 2D flow upstream of the salt screen, the mixing between the salt and fresh water layer downstream of the screen induces an inhomogeneous flow [42] with a stronger three-dimensional character. It is hypothesized that the difference in light sheet thicknesses of the LED and laser combined with the flow variation over the width of the channel is one of the sources that contribute to the deviations as observed in the plots on the right-hand side of Fig. 16.

4. Discussion

In this study focus has been put on the application of LED array illumination for PIV measurements in large-scale hydraulic laboratories as an alternative to class-4 pulsed lasers. The main difference is that LEDs generate a much less intense light sheet which tends to diverge much stronger than a laser sheet. To enable a sufficient intense imaging of tracer particles LED-based PIV measurements demand a relatively large illumination time, which can result in motion blur of the imaged particles. A theoretical analysis is performed to study the influence of motion blur (represented by the motion blur parameter β_{mb}) and PIV measurements are performed to investigate the applicability of LED arrays for two different large-scale hydraulic model setups.

From the theoretical analysis it is shown that increasing the illumination time up to conditions of moderate to strong motion blur (i.e. conditions that correspond to a motion blur parameter larger than 2) does not increase the intensity of an imaged particle and therefore will not result in an improvement of the reliability of the PIV analysis. The value of the motion blur parameter corresponds well to the maximum value of 5-pixel as proposed in literature [32] for the point spread function to avoid large errors in PIV measurements. Moreover, it is shown that the magnitude of time- and space-averaged flow velocities

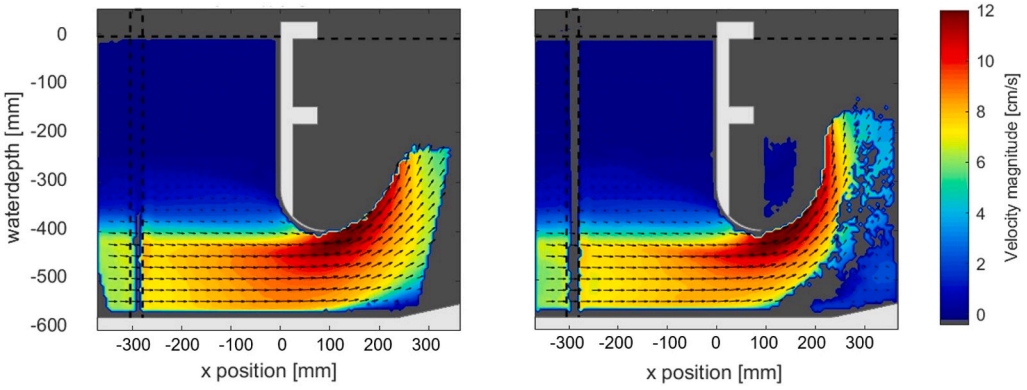

Fig. 15. Vector fields of time-averaged PIV results of the flow up- and downstream of the salt screen, obtained using (left) pulsed laser illumination and (right) continuous LED illumination. Averaged vectors are plotted for locations where at least 95 % of the instantaneous data a valid vector is obtained. The vertical region at x ~-300 mm is outlined and not taken into account in the PIV analysis since this is optically obstructed by a curve in the PMMA scale model.

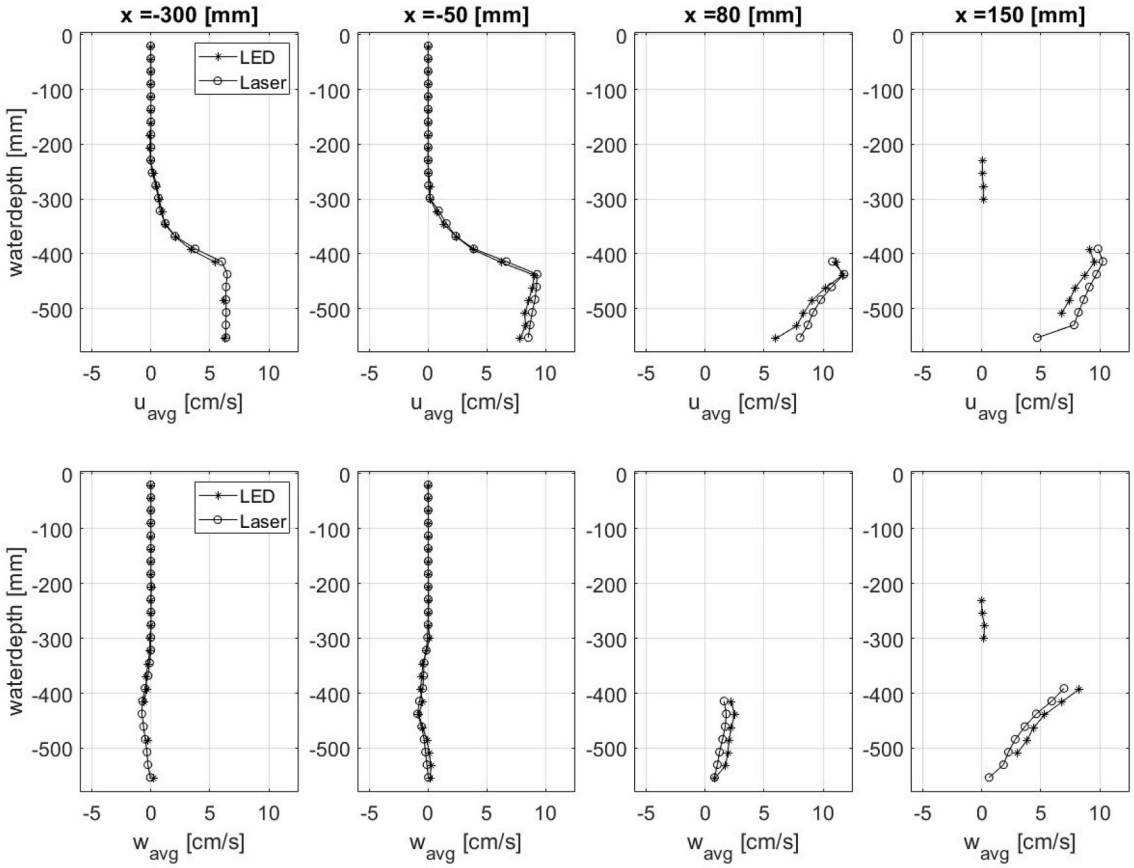

Fig. 16. Time-averaged velocity profiles of streamwise (top) and vertical (bottom) component for LED and laser-based PIV measurements at different upstream (x <80 mm and downstream (x >80 mm) locations with respect to the salt screen. Data corresponds to the vector fields shown in Fig. 15.

obtained in a LED-based PIV measurement decrease in case motion blur increases. This corresponds to the findings of earlier work on the influence of motion blur on the quality of PIV data [28] and is reminiscent of the known bias in PIV measurements towards lower velocity magnitude due to relatively fast tracer particles leaving the interrogation area [5]. Although the mechanisms which cause the observed PIV inaccuracies are not investigated in this study, previously it has been shown that main error sources in motion blurred PIV images are a low signal-to-noise-ratio, cross-correlation peak skewing or broadening and application of a.

Suboptimal sub-pixel estimator [28,31,32]. Additionally, motion blur has shown to negatively influence the accuracy of peak detection and thereby significantly increasing the number of outliers detected in the vector validation step of the PIV analysis [28]. While the size of the dataset in this study (obtained in the test case of the flow in a pump sump) is limited, it is expected that it is not possible to distinguish between the effects of the different motion blur error sources. Generally however, it can be stated that the application of LED-illumination for PIV measurements of high velocity flows becomes less attractive due to the effects of motion blur. However, for PIV measurements of low to moderate flows in which LED arrays are used, motion blur can generally be avoided in case the pulse width is set correctly (i.e. with a corresponding motion blur parameter smaller than 2).

Also for very large PIV measurement domains, the use of LEDs can serve as a valuable alternative to laser-based illumination, while the width of an LED light sheet can be increased by increasing the length of the LED array. It should however be noted that the LED arrays used in these tests consist of a large number of individual LEDs, resulting in a light sheet that is less intense at its edges, since a smaller number of individual LED bundles is overlapping as compared to the center of the LED light sheet (this is also shown to be the case for the pulsed LED array, as can be observed in the bottom subplot of Fig. 6). For future PIV applications in which an LED array is used, it is recommended to apply an LED array with a larger length than that of the measurement plane, thereby avoiding that the area of decreasing light intensity (the edges) is used in the PIV analysis. Moreover, specifically in the case of large measurement domains, the diverging character of LED arrays will result in a varying light sheet thickness throughout the field-of-view (the light sheet thickness increases with distance from the LED source). Although an in-depth analysis of the influence of such a variation on the accuracy of a PIV measurement is considered to be outside the scope of this study, some general remarks can be made. For instance, it is advised to apply the diverging LED arrays in predominantly 2D-flows to avoid large velocity gradients throughout the width of the light sheet. More generally, it can be stated that the light sheet thickness should be significantly smaller than the length scale of the relevant flow structures. A strongly diverging light sheet will also result in a strong decrease of light intensity with distance from the light source thereby reducing the signal-to-noise ratio. In case of a high-density of tracers, particles that are located at the backside of the light sheet might be blocked by illuminated particles that are located closer to the camera. Alternatively, the depth-of-field of the optical system can be set such that it is smaller than the light sheet thickness, thereby limiting the number of particles that are imaged in focus. To minimize the impact of spatial non-uniformity of light sheet intensity throughout the field-of-view in this study, the distance between the LED light source and the measurement plane was kept as small as possible to have the thinnest part of the light sheet in the field-of-view.

However, it should also be noted that the dataset as obtained from the measurements in the pump sump scale model only consists of 12 experimental conditions and is thus far from comprehensive. Although the measurements show a consistent (inversely proportional) relation

between motion blur and time-averaged flow velocities obtained from PIV measurements as was observed in previous work [28] it is still recommended to perform a more extensive experimental campaign in which only one parameter (preferably the exposure width of the LED) is varied, other than multiple (i.e. exposure width, flow velocity and interframe time) as is the case in the current work. Additionally, it would be relevant to further examine the influence of motion blur on higher order flow statistics (e.g. Reynolds stresses) as obtained from LED-based PIV data. Other than the test cases that are considered in this study it is advisable to perform such measurements in a canonical turbulent flow (e.g. grid-generated turbulence, taylor-couette flow, homogeneous isotropic turbulence, pipe flow, channel flow, jet flow, etc.) to quantify the effect of certain illumination properties. Comparison with reliable experimental and numerical data in such a reference testcase is recommended.

Note that the experiments were conducted with relatively large tracer particles of 100 μ m. For small-scale PIV measurements, smaller tracer particles are used (in the order of 1–10 μ m) which - due to their small reflective area-will be reflecting significantly less light and therefore demand either longer pulse widths (thereby possibly inducing image blur) or higher illuminance from the light source.

In the safety analysis it is shown that for the currently presented application of the used LEDs no hazards for the human eye- or skin are expected. The pulsed LED radiance levels can be increased by a factor of more than 10 before reaching the exposure limit for people in the close vicinity of the light source. It is expected that the ongoing development of LEDs will result in increasing luminosity, lifetime and reliability. Furthermore, development in LED collimators (for instance with gradient-index optics or 3D printed lenses) will provide improvements in light sheet conditions (i.e. less bundle divergence and higher illuminance due to a decrease in light-absorbance) and thereby will provide the applicability of LEDs as illumination source for PIV measurements of more complex flows (e.g. spatially inhomogeneous flows and high velocity flows). On the other hand, the development in lasers and laser diodes is ongoing, resulting in low-cost and high-quality coherent and collimated light sources, which may compete in the wider applicability of LEDs in optical measurement techniques. In literature, the application of such continuous wave lasers in a PIV system have been shown to provide accurate and reliable velocity field quantification of laminar Couette flow [43] and quantification of Reynolds stresses in a boundary layer [44]. However, since the most commonly illumination system of PIV are class 4 pulsed lasers [5], the application and light sheet properties of the LED arrays are compared to such pulsed lasers and the use of continuous wave lasers is not investigated in this work.

As mentioned in the introduction of this work, one of the advantages choosing LED line lights is their relatively low price. A double-pulsed laser as used in the test-case presented in this work of the stratified flow around a salt screen costs in the order of 50k€, while the LED line lights that are used are available for less than 10 % of that amount. Furthermore, the costs and workload of preparing a PIV measurement with LED-based illumination in certain large-scale setups (i.e. large hydraulic setups that are not located in a laser lab, like wave flumes and basins) can be significantly decreased due to a strong reduction in safety precautions that should be taken. From the safety analysis it is concluded that when applying a line array of LEDs much less safety precautions have to be taken as compared to a PIV setup where a class 4 pulsed laser is applied. Nevertheless, regardless of the type of illumination source, local shielding of a PIV setup in large scale-model facilities is generally needed to prevent ambient illumination influencing the light conditions at the measurement section.

5. Conclusions

In this work the application of LEDs as light source for planar PIV measurements in large hydraulic scale models has been investigated. The applicability of both pulsed and continuous arrays of LEDs are considered. A theoretical analysis is performed to determine the influence of the pulse width of the LED on the PIV images, characterized by the motion blur parameter β_{mb}, which is defined as the ratio between the length of an imaged particle during illumination and the diameter of a static particle image. From this theoretical approach it is concluded that an increase of the LEDs exposure time will not necessarily lead to a higher intensity of imaged particles. Generally, an increase in pulse width results in an increase in image blur. From the theoretical analysis it is suggested that it is not sensible to perform PIV measurements where the corresponding motion blur parameter is much larger than 2, as is also shown in an earlier study [28,32]. Measurements are conducted to determine the difference in light sheet conditions of (1) a conventional double-pulsed high intensity PIV laser, (2) a line array of pulsed LEDs equipped with a custom-made LED collimator and (3) a commercially available continuous LED line array with a relative strongly diverging light bundle. The light sheet properties obtained from these measurements are used in a theoretical safety analysis based on the international (eye) safety standards for lasers and incoherent light sources. It is found that the application of pulsed and continuous LEDs brings along significantly less strict safety precautions as compared to pulsed lasers for PIV purposes in experimental setups.

PIV measurements using LED illumination are compared to pitot tube measurements and conventional laser-based PIV measurements in two different hydraulic scale models. From the LED-based PIV measurements of a flow inside and around a scale-model of a bell mouth in a pump sump it is concluded that motion blur influences the spatially and temporally averaged flow velocities. A small, but consistent decrease in the measured velocity magnitude is observed for experiments characterized by an increasing value of the motion blur parameter. In this particular dataset, a decrease of 2 % of the (spatially and temporally averaged) vertical flow velocity is observed between the measurements with the most and least motion blur. Note that this “motion-blur effect” appears to have similarities to the known bias towards 2 % lower velocities in PIV measurements due to ‘fast’ tracer particles leaving the interrogation area [5], but should be considered as an additional bias. The results of the pump intake scale-model show that for a measurement domain of 0.3 m $\times$ 0.3 m a wide variety of flow conditions (bulk flow velocities ranging between 0.5 and 4 m/s) can be quantified with the use of a commercially available array of pulsed LEDs light source, which is equipped with a custom-made biconvex lens that acts as a collimator of the LED bundle.

From the scale-model tests of a stratified flow around a hydraulic structure it is concluded that, the diverging character of the LED light bundles does not affect the PIV measurements significantly. For moderate flow conditions with a strong two-dimensional character -such as found in the upstream part of the stratified flow test-case- the time-averaged results obtained with the LEDPIV measurements show good resemblance to the laser-based results. However, for higher flow velocities, such as in the suction pipe in the pump intake test-case the quality of the instantaneous data (represented by the percentage of valid vectors from the PIV analysis) is not as high as for conventional PIV measurements with laser illumination. Still, the time-averaged results show good resemblance with results obtained from conventional measurement instrumentation (i.e. pitot tube).

It is concluded that - even though the illuminance of LEDs is orders of magnitude smaller than that of pulsed high-power PIV lasers - the use of both pulsed and continuous LEDs for the test-cases gives similar results

of the time-averaged flow quantities as conventional flow measurement techniques. Specifically, LED arrays can serve as an alternative to laser illumination for PIV measurements in which low to moderate velocity fields (with a corresponding motion blur parameter smaller than 2) of predominantly two-dimensional flows are quantified. Moreover, in large hydraulic scale models where compliance to strict laser safety precautions is challenging (i.e. large hydraulic setups that are not located in a laser lab, like wave flumes and basins), the practical use of such LED arrays is advantageous over the application of class-4 laser-based PIV measurements.

CRediT authorship contribution statement

Wout Bakker: Writing – review & editing, Writing – original draft, Visualization, Validation, Resources, Methodology, Investigation, Formal analysis, Data curation. **Anton de Fockert:** Writing – review & editing, Supervision, Funding acquisition, Conceptualization. **Helena I. S. Nogueira:** Writing – review & editing, Supervision. **Gosse Oldenziel:** Writing – review & editing, Supervision, Project administration, Investigation, Formal analysis, Conceptualization.

Declaration of competing interest

The authors declare that they have no known competing financial interests or personal relationships that could have appeared to influence the work reported in this paper.

Acknowledgement

The authors would like to thank Prof. Dr. Ir. C. Poelma and Ing. E. Overmars, of the Laboratory for Aero- and Hydrodynamics at the Delft University of Technology for setting up this investigation and providing the possibility to use the LED line light to perform the measurements that are discussed in this paper. We would like to thank the Foundation for Fundamental Research on Matter (FOM, project: 15VAL11M) for their contribution in funding part of this investigation. Furthermore, the information and expertise obtained from a discussion with Dr. David Sliney and Eric van Rongen (both former members of ICNIRP) on the limits of eye- and skin exposure to LED light was found to be very valuable.

APPENDICES.

A1. Safe working conditions

A1i. Maximum permissible exposure

The maximum permissible exposure for laser and LED radiation exposure is given for three different safety hazards.

- Direct exposure to radiation at the cornea (MPE_c)
- Exposure to radiation at the cornea and retina from an extended source (viewing of diffuse reflections) (MPE_e)
- Direct exposure to radiation at the skin (MPE_s)

As the light sources are operated in the visible part of the light spectrum and intentional direct observation of the light source is not expected, the exposure duration is assumed to be limited by a natural aversion response of the eye, which is defined to be 0.25 s [26,45]. This value will be used as the maximum exposure time to estimate the MPE's for direct eye exposure to the different light sources. For the exposure from extended sources, the maximum exposure time for small light sources is 10 s, which is also set as the limit for direct exposure of skin to laser [6] and LED [30] radiation.

Pulsed laser. All MPE's regarding laser radiation are expressed in terms of the radiant exposure, which is defined as $H_e = Q_e{\cdot}k/A_p$, where Q_e is the radiant energy of the laser (in J per pulse), $k = 2.5$ is the MPE multiplication factor for a laser with an unknown mode structure [6] and A_p is the total projected area of the laser bundle (in m^2) at a certain distance x_s from the source, which is defined as $A_p = y_p{\cdot}z_p$. Where y_p and z are the length and height of the light sheet, which can be calculated using basic trigonometry, inserting the source's light sheet thickness (z_0) and length (y_0) and the divergence angles of the light sheet thickness (θ) and length (φ) respectively (as introduced in Fig. 4 and given in for the different light sources considered in this analysis). So, as the distance from the laser source increases, the projected area increases and therefore the radiant exposure decreases.

For the pulsed laser considered in this work, the MPE for direct ocular exposure (following the approach described in section 13.3 of [6]) is found to be 2.24 mJ/m^2. The limiting MPE of skin to exposure of the pulsed laser in this work is expressed in the irradiance (E_e) and (from table 8 of [6]) is listed as 2000 W/m^2. Note that E_e is defined as the mean irradiance during exposure at the skin.

Pulsed and continuous LED. Since the LEDs used in this work emit light in a narrow bandwidth around the peak wavelength of 530 nm, only the following three types of damage to the eye and skin are considered: 1) thermal damage of the retina; 2) "blue-light" photochemical damage of the retina; 3) thermal damage of the skin. For each damage type the effective radiance and/or radiant dose is compared to the exposure limits stated by ICNIRP [30]. The exposure limits for LEDs are expressed in the average (or effective) radiance L_e (in W/$m^2 \cdot$ sr) emitted. The radiance of a light source is defined as $L_e = \Phi_e/(A_0 \cdot \Omega_s)$ [45], where Φ_e is the radiant flux (or power) of the LED in W (not to be mistaken with the electrical input power of the light source), A_0 is the light emitting area of the source (so, equal to the product of y_0 and z_0) in m^2 and Ω_s is the solid angle of the emitted light bundle in steradian, which is defined as: $\Omega_s = A_p/x_s^2$, in which A_p is the total projected area of the LED bundle (equal to the product of y_p and z_p). The radiant flux Φ_e is het sum of the spectral radiant flux distribution of the LED $\Phi_{e,\lambda}$ (in W/nm) across the spectrum, or: $\Phi_e = \sum \Phi_{E,\lambda} \times \Delta\lambda$. The spectral radiant flux distribution is derived from the definition of the luminous flux [46]: $\Phi_V = K_M \sum_{380}^{780} \Phi_{E,\lambda} \times V(\lambda) \times \Delta\lambda$, where K_M ($\approx$ 683 lm/W) is the maximum luminous efficacy and $V(\lambda)$ is the photopic luminous efficiency function [47]. From these values, combined with the luminous flux of the LEDs (as listed in Table 1) the spectral radiant fluxes are found to be 5.15 W and 28.1 W for the pulsed and continuous LED arrays respectively. Combining these values with the light sheet characteristics (A_0 and Ω_s) gives the radiance of the two LED sources (which are listed in Table 3).

The effective retinal thermal radiance L_R (in W/($m^2 \cdot$ sr)) is defined as: $L_R = \sum_{380}^{1400} L_{e,\lambda}(\lambda) \times R(\lambda) \times \Delta\lambda$, where $L_{e,\lambda}(\lambda)$ is the distribution of the spectral radiance of the LED ($L_{e,\lambda}(\lambda) = \Phi_{E,\lambda}/(A_0 \cdot \Omega_s)$) and $R(\lambda)$ is the retinal thermal hazard function (as given in Table 2 of [30]) along the wavelength

bandwidth. Likewise, the effective blue-light photochemical radiance L_B and skin thermal radiance L_{skin} are defined: $L_B = \sum_{380}^{1400} \Phi_{e,\lambda}(\lambda) \times B(\lambda) \times \Delta\lambda$, where $B(\lambda)$ is the blue-light hazard function (as given in Table 2 of [30]) and $L_{skin} = \sum_{380}^{3000} \Phi_{e,\lambda}(\lambda) \times \Delta\lambda$. The radiance values for the LED sources are listed in Table 3.

Table 3
Radiance levels for the different LED sources

	L_e (W/(m^{2}sr))	L_R (W/(m^{2}sr))	L_B (W/(m^{2}sr))	L_{skin} (W/(m^{2}sr))
Pulsed LED	$1.92 \cdot 10^4$	$1.92 \cdot 10^4$	$6.37 \cdot 10^2$	$1.90 \cdot 10^4$
Continuous LED	$1.16 \cdot 10^5$	$1.16 \cdot 10^5$	$3.86 \cdot 10^3$	$1.11 \cdot 10^5$

For a first intuitive characterization of the hazards due to exposure of LED light, the obtained radiance levels (L_E) listed in Table 3 can be compared to the sun's radiance, which is $1.3 \cdot 10^7$ W/(m$^2 \cdot$ sr) at zenith (as listed in Tables 22-1 in Ref. [45]). Hence, the sun's radiance is more than 100 times larger than that of the LED arrays, which is a first indication that being exposed to radiance levels associated to the LED arrays considered in this investigation is non-hazardous to the human eye and skin.

A1ii. Nominal Ocular Hazard Distance and Hazard Distance

To determine the distance from which radiant exposure is considered to be harmless, (known as the *Nominal Ocular Hazard Distance* (NOHD) and *Hazard Distance* (HD) for eye and skin exposure respectively), estimates of direct and indirect exposure to the light sources are compared with the appropriate MPE's [6] and exposure levels [30] for the laser and LEDs respectively. For direct ocular exposure, the NOHD for the pulsed laser sheet is calculated to be 320 m, while for the pulsed and the continuous LED both the blue-light and thermal radiance levels remain orders of magnitude below the prescribed exposure limits for the human eye (in addition to the radiance levels listed in Table 3, radiance dose and radiant exposure were also found to be much smaller than the stated exposure limits) [30]. The same yields for direct exposure of both pulsed and continuous LED light to the skin. For the laser sheet on the other hand, the hazard distance is found to be 2.2 m.

For the exposure from extended sources, the following situation is considered: a test setup with a light source is covered with sheltering material. A person standing in the vicinity of the setup is exposed to light that is reflected twice: first specular reflection of the light source occurs on an aluminum beam (with reflectance $R_1 = 0.9$) at a distance of 2 m from the light source located in the sheltered space, followed by diffuse reflection on an opaque surface (reflectance $R_2 = 0.5$ and diffuse angle $\varphi_{ref} = 10$ deg.) located at a distance of 1 m from the metal beam causing the light radiating outside the sheltered setup. The NOHD of such an extended source is estimated from the reflected radiant exposure H_{ref}, which, for the pulsed laser is defined as:

$$H_{ref} = Q_1 \cdot R_1 \cdot R_2 \,/\, \left(A_{ref} + \pi \cdot \left(x_{ref} \cdot \tan\left(\varphi_{ref} \,/\, 2\right)\right)\right) \tag{1}$$

where Q_1 is the radiant energy of the light source at the aluminum beam (in J/m^2), A_{ref} is the size of the diffuse reflective area (in this example set to 0.01 m^2) and x_{ref} is the distance between the observer and the diffuse reflection (in m). For the LED, the reflected radiance (L_{ref}) and radiance dose (D_{ref}) can be estimated analogously by substituting L_1 and D_1 into Q_1 in equation (1) respectively. For the pulsed laser sheet, the NOHD is found to be 6.2 m, which is significantly smaller than the NOHD for direct ocular exposure, but still means that extensive safety precautions should be taken, such as closure of the area surrounding the experimental setup or the application of laser safety materials and utilities (such as laser safety goggles for people working in the vicinity of the setup and shielding material to prevent exposure to laser light).

Data availability

Data will be made available on request.

References

[1] J. Anderson, Computational Fluid Dynamics: the Basics with Applications, Springer, Berlin Heidelberg, 2009.
[2] J. Aberle, C. Rennie, D. Admiraal, M. Muste, Experimental hydraulics: methods, instrumentation, data processing and management. Volume II: Instrumentation and Measurement Techniques, CRC Press, Boca Raton, 2020.
[3] C. Tropea, A. Yarin, J.F. Foss, Springer Handbook of Experimental Fluid Mechanics, Springer-Verslag Berlin Heidelberg, Berlin, 2007.
[4] R.J. Adrian, Twenty years of particle image velocimetry, Exp. Fluid (2005) 159–169.
[5] R.J. Adrian, J. Westerweel, Particle Image Velocimetry, Cambridge University Press, New York, 2011.
[6] IEC, IEC 60825-1 International Standard, Safetey of Laser Products, International Electrotechnical Commission, Genéve, 2014.
[7] M. Raffel, C. Willert, F. Scarano, C. Kähler, S. Wereley, J. Kompenhaus, in: Particle Image Velocimetry: A Practical Guide, third ed., Springer-Verlag Berlin, Heidelberg, 2007.
[8] V. Weitbrecht, G. Kühn, G. Jirka, Large scale PIV-measurements at the surface of shallow water flows, Flow Meas. Instrum. 13 (2002) 237–245.
[9] M. Jodeau, A. Hauet, A. Paquier, J. Le Coz, G. Dramais, Application and evaluation of LS-PIV technique for the monitoring of rive rsurface velocities in high flow conditions, Flow Meas. Instrum. 19 (2008) 117–127.
[10] I. Murgan, F. Bunea, G. Dan Ciacan, Experimental PIV and LIF characterization of a bubble column flow, Flow Meas. Instrum. 54 (2017) 224–235.
[11] B. Stasicki, J. Kompenhans, C. Willert, K. Ludwikowski, Pulsed LED illuminator for visualization, Recording and measurement of high-speed Events in mechanics, Exp. Fluid (2014) 141–147.
[12] J.S. Sousa, F. Carneiro, N. Viriato Ramos, P.J. Tavares, P.M.G.P. Moreira, Development of LED-based illumination system for high-speed digital image correlation, Procedia Struct. Integr. (2019) 828–834.
[13] W. Bakker, F.I.H. Verhaart, A. de Fockert, G. Oldenziel, Pulsed light emitting diodes for particle image velocimetry in a vertically submersible pump, in: *38th IAHR World Congress*, Panama City, 2019.
[14] C. Willert, S. Moessner, J. Klinner, Pulsed operation of high-power light emitting diodes for imaging flow velocimetry, Meas. Sci. Technol. (2010) 1–11.
[15] D. Gross, W. Brevis, G.H. Jirka, Development of a LED-based PIV/PTV system: characterization of the flow within a cylinder wall-array in a shallow flow, in: *River Flow: International Conference on Fluvial Hydraulics*, Branschweig, 2010.
[16] W. Bakker, B. Hofland, E. de Almeida, E. Overmars, G. Oldenziel, Pulsed LED line light for large-scale PIV - development and use in wave load measurements, Meas. Sci. Technol. 32 (2021) 1–12.
[17] S. Hochstein, A. Jakupov, J.-U. Schmollack, D. Sporer, V. Wank, R. Blickhan, An alternative illumination source based on LEDs for PIV measurements on human swimmers—a feasibility study, Flow Meas. Instrum. 88 (2022).
[18] A. Kloosterman, B. Hierck, J. Westerweel, C. Poelma, Quantification of Blood flow and Topology in developing vascular Networks, PLoS One (2014) 1–13.
[19] R. Lindken, M. Rossi, S. Grosse, J. Westerweel, Micro-particle image velocimetry (μPIV): recent developments, applications, and guidelines, Lab Chip (2009) 2551–2567.
[20] H. Nasibov, E. Balaban, A. Kholmatov, A. Nasibov, High-brightness, high-power LED-based strobe illumination for double-frame micro particle image velocimetry, Flow Meas. Instrum. (2014) 12–28.
[21] N.A. Buchmann, C.E. Willert, J. Soria, Pulsed, high-power LED illumination for tomographic particle image velocimetry, Exp. Fluid (2012) 1545–1560.

[22] F. Huhn, D. Schnza, P. Manovski, S. Gesemann, A. Schröder, Time-resolved large-scale volumetric pressure fields of an impinging jet from dense Lagrangian particle tracking, Exp. Fluid (2018) 59–81.
[23] D. Schanz, F. Huhn, S. Gesemann, U. Dierksheid, R. van de Meerendonk, P. Manovksi, A. Schröder, Towards high-resolution 3D flow field measurements at cubic meter scales, in: 18th International Symposium on the Application of Laser and Imaging Techniques to, Fluid Mechanics, Lisbon, 2016.
[24] I. Viola, A. Nila, T. Davey, R. Gabl, Underwater LED-based Lagrangian particle tracking velocimetry, J. Visual 25 (2022) 1035–1046.
[25] J. Estevadeordal, L. Goss, PIV with LED: particle shadow velocimetry (PSV), in: 43rd AIAA Aerospace Sciences Meeting and Exhibit, Reno, Nevada, 2005.
[26] ICNIRP, Light-emitting diodes (LEDS): implications for safety, Health Phys. 118 (5) (2020) 549–561.
[27] A. von Lühmann, C. Herff, D. Heger, T. Schultz, Toward a Wireless open source instrument: Functional Near-infrared Spectroscopy in Mobile Neuroergonomics and BCI applications, Front. Hum. Neurosci. (2015) 229–242.
[28] J. Oh, H. Lee, W. Hwang, Motion blur treatment utilizing deep learning for time-resolved particle image velocimetry, Exp. Fluid 62 (234) (2021).
[29] M. Stanislas, J. Westerweel, J. Kompenhans, Particle Image Velocimetry: Recent Improvements, Zaragoza, Spain, 2003.
[30] ICNIRP, On limitis of exposure to incoherent visible and infrared radiation, Health Phys. (2013) 74–96.
[31] G.E. Elsinga, B.W. van Oudheusden, S. F, The effect of particle image blur on the correlation map and velocity, in: *Proceedings of SPIE*, San Diego, 2005.
[32] W. Thielicke, Pulse-length induced motion blur in PIV particle images: to be avoided at any cost?, in: *Fachtagung "Experimentelle Strömungsmechanik"*, Ilmenau, 2022.
[33] G. Wang, L. Wang, F. Li, G. Zhang, Collimating lens for light-emitting-diode light source based on non-imaging optics, Appl. Opt. 51 (11) (2012) 1654–1659.
[34] A.M. McCarthy, J. Romereo-Vivas, C. O'Hara, N. Rebrova, L. Lewis, S.P. Hegarty, LED based collimating line-light combining freeform and Fresnel optics, IEEE Photon. J. 10 (6) (2018) 1–13.
[35] D. Fiscaletti, J. Westerweel, G. Elsinga, Long-range μPIV to resolve the small scales in a jet at high Reynolds number, Exp. Fluid 55 (1812) (2014) 1–18.
[36] J. Keller, G. Möller, R.M. Boes, PIV measurements of air-core intake vortices, Flow Meas. Instrum. 40 (2014) 74–81.
[37] ANSI, ANSI/HI 9.8-2018, American National Standard for Rotodynamic Pumps for Pump Intake Design, Hydraulic Institute, Parssipany, NJ, 2018.
[38] F.I.H. Verhaart, A. de Fockert, S. Zwanenburg, Velocity profiles in the bell mouth throat of vertically submersible pumps, Journal of Applied Water Engineering and Research (2015) 102–111.
[39] A. de Fockert, F. Verhaart, F. Ferdos, Experimentally determined effect of swirl on the performance of a rotodynamic pump, J. Hydraul. Res. 60 (3) (2022) 434–444.
[40] J. Westerweel, F. Scarano, Universal outlier detection for PIV data, Exp. Fluid 39 (6) (2005) 1096–1100.
[41] R. Ettema, D. Zhu, S. Gaskin, S. Mulligan, T. Lyons, R. Boes, S. Chan, J. Lee, Vortex-Flow Intakes, IAHR Water Monograph Series, International Association for Hydro-Environment Engineering and Research, 2025.
[42] A. de Fockert, T. O'Mahoney, H. Nogueira, G. Oldenziel, A. Bijlsma, H. Janssen, Assessing the Effectiveness of the IJmuiden salt screen design for nonuniform selective withdrawal by physical and numerical modeling, J. Hydraul. Eng. 148 (2) (2022).
[43] C. Willert, High-speed particle image velocimetry for the efficient measurement of turbulence statistics, Exp. Fluid 56 (17) (2015) 1–17.
[44] L. Luberto, K. de Payrebrune, Examination of laminar Couette flow with obstacles by a low-cost particle image velocimetry setup, Phys. Fluids 33 (2021).
[45] D. Sliney, M. Wolbarsht, Safety with Lasers and Other Optical Sources, Plenum Press, New York, 1980.
[46] CIE, Standard CIE S 017/E:2011 ILV: International Lighting Vocabulary, International Commission on Illumination (CIE), Vienna, Austria, 2011.
[47] CIE, CIE 1931 Colour-Matching Functions , 2 Degree Observer, International Commission on Illumination (CIE), Vienna, Austria, 2018.